FAKULTA
STROJNÍ
ČVUT V PRAZE

Ústav letadlové techniky

Měřicí stav pro charakterizaci pohonů nanodružic

Thrust stand for characterization of nanosatellite propulsion

DIPLOMOVÁ PRÁCE

2022

Michal KOCOUREK

Studijní program: N3958 LETECTVÍ A KOSMONAUTIKA
Studijní obor: 2301R000 Studijní program je bezoborový
Vedoucí práce: Mgr. Jaroslav Kousal Ph.D.

ZADÁNÍ DIPLOMOVÉ PRÁCE

I. OSOBNÍ A STUDIJNÍ ÚDAJE

Příjmení: **Kocourek** Jméno: **Michal** Osobní číslo: **474840**

Fakulta/ústav: **Fakulta strojní**

Zadávající katedra/ústav: **Ústav letadlové techniky**

Studijní program: **Letectví a kosmonautika**

Studijní obor: **Letadlová a kosmická technika**

II. ÚDAJE K DIPLOMOVÉ PRÁCI

Název diplomové práce:

Měřicí stav pro charakterizaci pohonů nanodružic

Název diplomové práce anglicky:

Thrust stand for characterization of nanosatellite propulsion

Pokyny pro vypracování:

1) Proveďte rešerši mechanických aspektů používaných konstrukčních řešení měření malých tahů (uN-mN) ve vakuu.
2) Stanovte konstrukční limity a provozní podmínky pro možnou realizaci měření tahů v rozsahu 100uN-2mN. Zohledněte stávající možnosti pracoviště.
3) Zhodnoťte používané konstrukční principy a stanovte základní koncepci měřicího stavu.
4) Vypracujte předběžný konstrukční návrh měřicího stavu a výpočty zhodnoťte dosažitelnou přesnost měření.

Seznam doporučené literatury:

J. E. Polk, A. Pancotti, T. Haag, S. King, M. Walker, J. Blakely, J. Ziemer, Recommended Practice for Thrust Measurement in Electric Propulsion Testing, Journal of Propulsion and Power, vol. 33, no. 3, 2017 + další literatura dle doporučení vedoucího

Jméno a pracoviště vedoucí(ho) diplomové práce:

Mgr. Jaroslav Kousal, Ph.D. ústav letadlové techniky FS

Jméno a pracoviště druhé(ho) vedoucí(ho) nebo konzultanta(ky) diplomové práce:

Datum zadání diplomové práce: **29.04.2022** Termín odevzdání diplomové práce: **08.06.2022**

Platnost zadání diplomové práce: _____

Mgr. Jaroslav Kousal, Ph.D.	Ing. Robert Theiner, Ph.D.	doc. Ing. Miroslav Španiel, CSc.
podpis vedoucí(ho) práce	podpis vedoucí(ho) ústavu/katedry	podpis děkana(ky)

III. PŘEVZETÍ ZADÁNÍ

Diplomant bere na vědomí, že je povinen vypracovat diplomovou práci samostatně, bez cizí pomoci, s výjimkou poskytnutých konzultací. Seznam použité literatury, jiných pramenů a jmen konzultantů je třeba uvést v diplomové práci.

. _____ Datum převzetí zadání

_____ Podpis studenta

PROHLÁŠENÍ

Prohlašuji, že jsem diplomovou práci s názvem: „Měřicí stav pro charakterizaci pohonů nanodružic“ vypracoval samostatně pod vedením Mgr. Jaroslava Kousala, Ph.D. a s použitím literatury uvedené na konci mé diplomové práce v seznamu použité literatury.

DECLARATION

I declare that this thesis, by the name “Thrust stand for characterization of nanosatellite propulsion” was created solely by me, with the help of my thesis supervisor Mgr. Jaroslav Kousal, Ph.D. and the literature provided at the end of this thesis in the list of references.

Prague ....

Michal Kocourek

PODĚKOVÁNÍ

Rád bych zde poděkoval vedoucímu mé diplomové práce, Mgr. Jaroslavu Kousalovi, Ph.D. za jeho vedení a čas, který mi věnoval. Dále bych rád poděkoval vyučujícím Ústavu letadlové techniky, zejména Ing. Aleši Kratochvílovi, Ph.D. za zapůjčení vybavení, odborné rady a pomoc při měření hluku prostředí.

ACKNOWLEDGEMENT

I would like to thank my thesis supervisor Mgr. Jaroslav Kousal, Ph.D. for his guidance and the time he spent helping me with my thesis. I would also like to thank the teachers of the Department of Aerospace Engineering, primarily Ing. Aleš Kratochvíl, Ph.D. for the borrowing of equipment, expert advice and help with the measurement of the noise of the environment.

ANOTAČNÍ LIST

Jméno autora:	Micha Kocourek
Název DP:	Měřicí stav pro charakterizaci pohonů nanodružic
Anglický název:	Thrust stand for characterization of nanosatellite propulsion
Zadávající ústav:	Ústav letadlové techniky
Vedoucí DP:	Mgr. Jaroslav Kousal Ph.D.
Bibliografické údaje:	Počet stran 51
	Počet obrázků 30
	Počet tabulek 7
	Počet příloh 1
Klíčová slova:	Pohon nanodružic, měřicí stav, kyvadlo
Keywords:	Nanosatellite propulsion, thrust stand, pendulum
Anotace:	Tato diplomová práce se zabývá předběžným vývojem měřícího stavu pro charakterizaci pohonů nanodružic, použitelného v objektu zadávajícího ústavu. Různé používané přístupy byly nalezeny v literatuře a porovnány s podmínkami v objektu ústavu k vytvoření předběžného návrhu. Předběžný návrh ukazuje slibnou přesnost vzhledem k očekávaným rozsahům tahu.
Annotation:	This master's thesis deals with a preliminary design of a thrust stand for characterization of nanosatellite propulsion suitable for facility of the submitting department. Various commonly used approaches were found in the literature and compared with the conditions at the facility for the creation of a preliminary design. The preliminary design shows promising accuracy with regard to the expected thrust ranges.

Table of Contents

1. Introduction

For space applications, the key characteristics of propulsion include a specific impulse and thrust. For a given propellant mass, the specific impulse is proportional to the total velocity change that a thruster can achieve. Thrust is inversely proportional to the time necessary for the velocity change. The power consumed by a thruster is proportional to the product of the two characteristics. This implies that thrusters with very high specific impulse often have very low thrust, and therefore, low thrust to weight ratio. This makes it difficult to measure the thrust since regular thrust stands would be predominantly loaded with the thruster weight rather than its thrust. The aim of this thesis is to outline a possible approach to micro-thrust measurement for the facility of the Department of Aerospace Engineering at the Faculty of Mechanical Engineering of the Czech Technical University in Prague (FME CTU).

Construction principles of micro-thrust measurement that are practically used were reviewed, and specific components used for the thrust stands were examined to give us a better understanding of the possible solutions.

Working conditions and construction limitations were determined. An experiment was set to measure the noise of the environment under various setups. The probable causes of individual frequencies of the noise were investigated to enable effective reduction of the noise.

The suitability of the various approaches used for micro-thrust measurement for the given working conditions and construction limitation was compared and the best suitable design principle was selected for the thrust stand.

Finally, a preliminary design was created based on the selected design principle. An optimal configuration for high sensitivity and low mass was proposed. Parasitic forces entering the system associated with each component were inspected and the resultant sensitivity was calculated.

2. State of the art

This chapter discusses approaches to the problem as a whole and to certain specific aspects of the problem found in the literature.

2.1. Measurement principles

In this chapter, the methods used in literature for micro thrust measurement are discussed. Those methods include direct thrust measurement, impulse bit measurement and exhaust plume momentum measurement.

2.1.1. Direct Thrust Measurement

Direct thrust measurement generally utilizes the principle of a pendulum, where the deflecting effect of the small thrust of the thruster is magnified by a long pendulum arm. The thrust changes the balanced position of the steady state. The displacement of the pendulum is proportional to the thrust. There are three main pendulum configurations: a hanging pendulum, an inverted pendulum, and a torsional pendulum. All generally consist of a pendulum arm, a torsion spring or a flexural pivot, a device for deflection measurement, and often a damper. The individual components are discussed in more detail in chapter 2.2.

2.1.1.1. Hanging Pendulum

The hanging pendulum is the configuration of a classical pendulum, with the thruster mounted below the point of rotation. The simplest form is shown in Figure 1. The main advantage of this configuration is that the design is relatively simple, and it is easy to use. Another advantage is that it is inherently stable, and therefore it does not necessarily need a spring element to act as a force to restore it to the null position. [1] [2] [3] [4] [5]

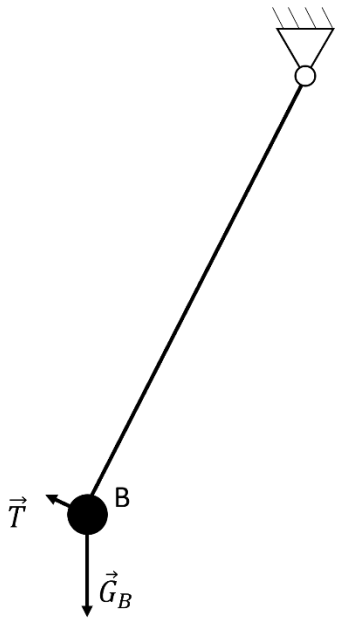

Figure 1 - Hanging pendulum in its simplest form.

2.1.1.2. Inverted Pendulum

The design of an inverted pendulum is similar to that of a hanging pendulum, with the difference that the thruster is mounted above the point of rotation. The weight of the thruster amplifies the deflection with a torsion spring acting as the restoring force. The advantage of this configuration is high sensitivity. Relatively high deflections can be achieved even with very low thrust. The disadvantage is that it is inherently unstable. This makes it very sensitive to external influences such as temperature (which can affect the stiffness of the torsion spring), the environmental noise, or the inclination of the stand with respect to the gravity vector. [1] [2] [3] [4] [5]

2.1.1.3. Torsional Pendulum

In this configuration, the axis of rotation is parallel to the gravity vector. The thruster and a counterweight rotate around a torsion beam or a flexural pivot. This configuration is not directly dependent on the weight of the thruster, although it must be considered in dimensioning the pivot. It offers a compromise between high thrust stand sensitivity and low environmental noise sensitivity. For high sensitivity, it is necessary to have a long beam, and therefore a large vacuum chamber. [1] [2] [3] [4] [5]

2.1.2. Impulse Bit Measurement

The construction of the stands for impulse bit measurements is the same as for the direct thrust measurement, but it works with a different measurement principle. The thruster uses individual impulse bits with accordance with the natural frequency of the stand. The resonance amplifies the deflection significantly, so it is possible to measure even very low impulse bits.

It is, therefore, very important to accurately characterize the dynamics of the thrust stand. [1]

2.1.3. Exhaust Plume Momentum

Reactive thrusters generate their thrust as a result of a change of the momentum of a propellant:

$$\vec{T} = \dot{m} \cdot \vec{v}_e, \tag{1}$$

where $\vec{T}$ is the thrust, $\dot{m}$ is the mass flow of the propellant, and $\vec{v}_e$ is the effective exhaust velocity.

Therefore, if you can accurately measure the momentum of the propellant exiting the thruster, you can easily determine the thrust. The main challenge of this method is ensuring sufficient accuracy of the momentum measurement.

The most common principle of the momentum measurement is directing the exhaust plume on a pendulum arm with a target plate. The exhaust plume is reflected from the target plate exerting force and the target plate is deflected.

This principle has been utilized in [6], where the target plate is a carbon composite rectangle hanging on two lines. Its deflection is measured by a laser triangulation sensor.

This design has several drawbacks. The main drawback is that although the experiment is conducted in a vacuum chamber, there are still residual gas particles with which the exhaust plume interacts. The pressure in the vacuum chamber used in [6] was expected to be approximately 10^{-2} Pa. At this pressure level, the particle density is still relatively high ($2.45 \cdot 10^{18}$ m^{-3}) For this reason, it was considered rather a thrust verification than a measurement.

Accurate measurement can be accomplished with higher vacuums and more detailed examination of the exhaust plume. This has been demonstrated in [7], where a series of compensating elements have been implemented to reduce the measurement error.

2.2. Components

Some components of the thrust stands are common across the different designs. Some share only the principal purpose and other are unique for the specific designs. The most common components are discussed in this chapter.

2.2.1. Pendulum Arms

Pendulum arms are essential structural components of the stand. Higher rigidity can be either beneficial or detrimental based on the specific design. For the inverted pendulums, bending of the pendulum arm causes an additional gravity torque at the spring element which could lead to instability. On the other hand, if multiple pendulum arms are used for better stability, any manufacturing inaccuracy blocks rigid body motion. This phenomenon is discussed in more detail in Chapter 5.2.1.

Fishing lines can be used for target plates for exhaust plume momentum measurement or for the hanging pendulums. The resistance of a fishing line can be lower than that of a pivot, but this design renders any use of counterweight impossible.

2.2.2. Spring Element

The spring element of the thrust stand includes a pendulum pivot and the springs added to increase the stiffness of the mechanism. Wires and tubing may also be included, as their stiffnesses also contribute to the stiffness of the whole mechanism.

Simple flat plate flexures or more complex flexural pivots can be used as the pendulum pivots. Knife edge pivots are sometimes used to minimize the restoring force.

Spring elements are crucial for inverted pendulums because their torque must be higher than the gravity torque, but any margin decreases the sensitivity.

For torsional pendulums, the lower the stiffness of the spring element, the higher the sensitivity of the thrust stand. This often leads to the utilization of long beams which increase the spatial requirements for the vacuum chamber. Thin beryllium or tungsten wires are sometimes used.

Hanging pendulums are inherently stable, so no springs are needed to increase the stiffness of the mechanism. Springs could, in theory, be used in the reversed position to act against the gravity torque, although no examples of this application were found in the literature.

For wires and tubing it is important to decrease the stiffness and/or to ensure sufficient repeatability, so that their influence is accurately included in the overall stiffness during the calibration.

2.2.3. Displacement sensor

The choice of the displacement sensor depends mostly on the expected order of the displacement. Table 1 shows some linear and angular displacement sensors used for thrust stand applications and their typical accuracies.

Table 1 - Linear and angular displacement sensors and their typical accuracies.

Displacement sensor	Linear/Angular	Typical accuracy
LVDT	Linear	± 5 μm [1] [8]
RVDT	Angular	± 1 % FS (Full scale) [9]
Capacitive sensor	Linear	Up to 0.02 % FS [10]
Optical interferometer	Linear	8.5 parts in 10^8 [11]
Reflectance fiber optic sensor	Linear	5 nm [12]
Autocollimator	Angular	Up to 48.5 nrad [1]
Laser triangulation system	Linear	Up to 0.5 μm [13]
Photoelectric position system	Linear	20 μm [14]

2.2.4. Damper

Passive or active, PID controlled dampers are incorporated to damp the oscillations of the thrust stand and to help it to reach the steady state faster. Eddy current dampers are the most common passive dampers. Their construction generally consists of two permanent magnets and a conductive, nonmagnetic plate. The oscillations of the magnets generate a changing magnetic field which induces eddy currents in the plate. The energy of the oscillations is transformed into the eddy currents and dissipated into heat [15] [16].

Viscous oil dampers are sometimes used as an alternative. Thorough insulation is necessary, so that the oil does not contaminate the vacuum pump. [1]

Active dampers use closed loop PID controlled electromagnets and enable frequency dependent damping effects. Active dampers can be turned off for impulse bit measurements [1].

2.2.5. Vibration Isolation

A reasonable estimate of the mechanical noise is 0.025 mm [1]. This limits the effectivity of very precise displacement measurement. For this reason, vibration isolation may be implemented.

The general principle of passive vibration isolation is simple. The payload is connected to the vibrating base by a spring element and a damping element (often the same part). The spring stiffness and the damping coefficient are chosen according to the characteristics

of the vibration and the mass of the payload. The typical damping elements include air dampers, oil dampers, spring dampers, rubber dampers, negative stiffness vibration isolators, etc. [17]

The technology of passive vibration isolation was perfected for the gravitational waves' measurement at LIGO, where the measured displacement is in the range of 10^{-19} m. The 40 kg LIGO mirrors hang on a 360 kg quadruple-pendulum system, where each successive mass is connected by thin silica fibers (Figure 2). This system itself is placed beneath an active vibration isolation system which damps out larger amplitude (e.g., seismic) vibrations. [18]

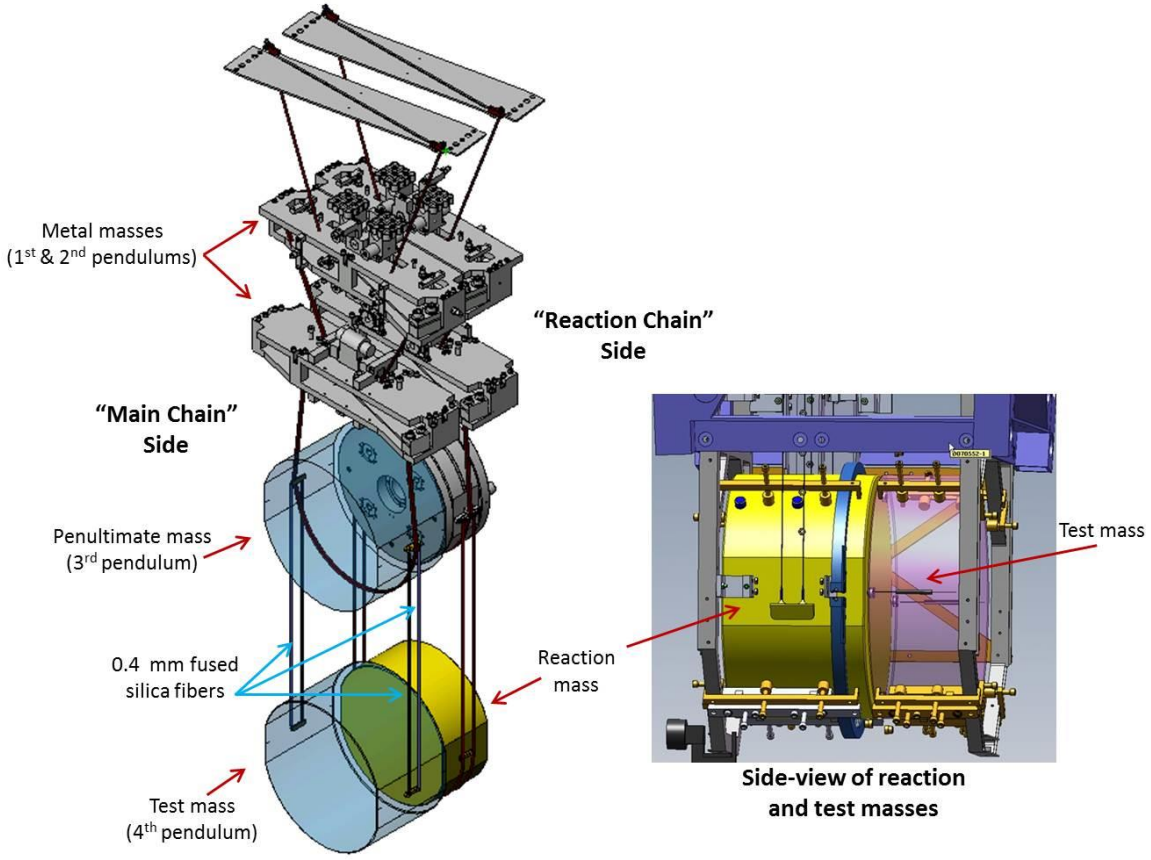

Figure 2 - LIGO quadruple-pendulum vibration isolation system [18].

Active vibration isolation consists of a vibration sensor an actuator and a controller. Typical sensors are accelerometers or optical sensors. Those provide an input typically for a PID controller which drives an electromagnetic actuator. [1]

2.3. Calibration

Although the response of the thrust stand can be calculated and/or simulated, it is strongly advised to calibrate the thrust stand to verify and refine the calculated response. On steady state thrust stands, the calibration is done by applying a known force on the thruster. Typically, several points of different thrust magnitude are measured, and the force-displacement relation is interpolated from these values. Extrapolation can also be

used, if necessary, although the error may be far more significant, especially for lower forces, where the relative effect of i.e., friction becomes considerable.

An example of known force application is described in [1]. Here, the known forces are applied by a pulley system and a motor-driven spool, which loads, and unloads known weights. The applied calibration forces were in the order of tens of millinewtons. The diagram of the setup is shown in Figure 3.

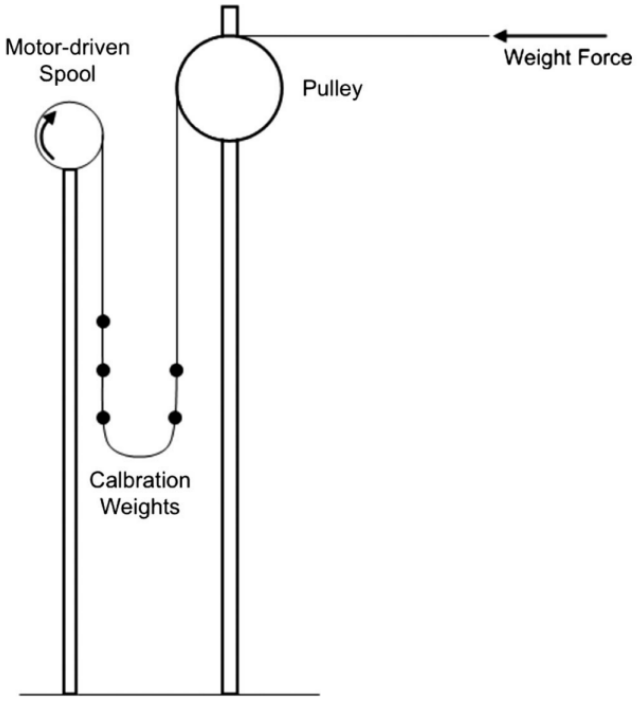

Figure 3 - Pulley system calibration setup [1].

Calibration of the thrust stands for impulse bit measurement is a little sophisticated because it is necessary to characterize the dynamical behavior of the thrust stand. The response over the appropriate range of applied known impulse bits must be characterized. There are various methods to of contact and noncontact application of known impulses. Contact methods include the swinging of known masses or the use of impact pendulums or impact hammers. Examples of noncontact methods are calibration using electrostatic forces between planar electrodes, free molecular gas flow from underexpanded orifices, electrostatic combs, and electromagnetic coils. [1]

3. Working conditions

To successfully design a thrust stand, the construction limits and working conditions must first be assessed. The most important parameters that determine the design of the thrust stand are the shape and dimensions of the vacuum chamber, the minimal pressure that can be achieved, and the noise of the environment.

3.1. Vacuum Chamber

The Department of Aerospace Engineering at the Faculty of Mechanical Engineering of the Czech Technical University in Prague (FME CTU) has two vacuum chambers available. The larger of the two has a diameter of 400 mm and length of 1000 mm. Because the space is such an important limiting factor, the smaller one is no longer considered.

The larger vacuum chamber is supported by a construction of aluminum profiles, and it does not have any kind of isolation from the noise of the environment or any control of inclination. The construction has wheels, which enable easy manipulation, but at the same time the repeatability of the inclination can, therefore, not be ensured.

The chamber has openings in the bases of the cylinder and in planes located 250 mm from each base. A simplified CAD model is shown in Figure 4. Openings suitable for the vacuum pump are marked blue on the figure.

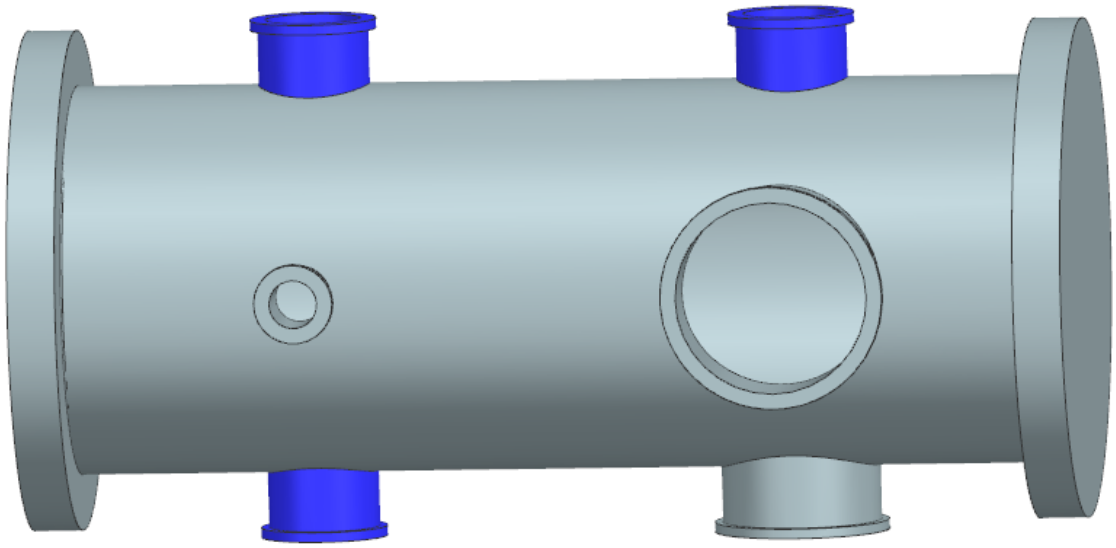

Figure 4 - A simplified CAD model of the vacuum chamber with the openings suitable for the vacuum pump.

Both a vertical and a horizontal arrangement of the vacuum chamber can be considered (Figure 5).

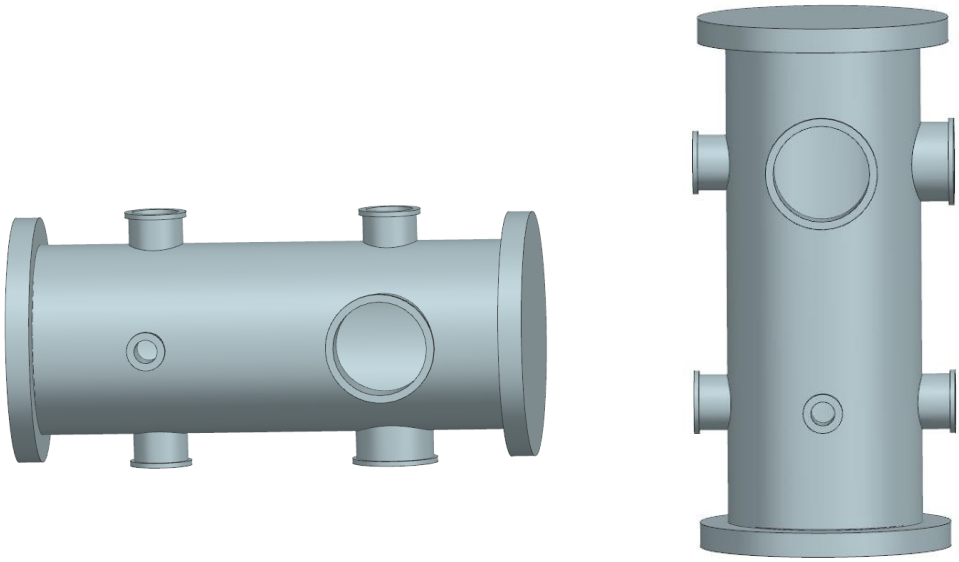

a) Horizontal *b) Vertical*

Figure 5 - The horizontal and vertical orientation.

3.2. The Supporting Construction

A simple experiment was carried out to determine the approximate natural frequencies of the construction. Only the two main flexural modes of the rectangular construction were inspected. The acceleration was measured by a mobile phone with a BOSCH BMI160 accelerometer. The setup is shown on Figure 6.

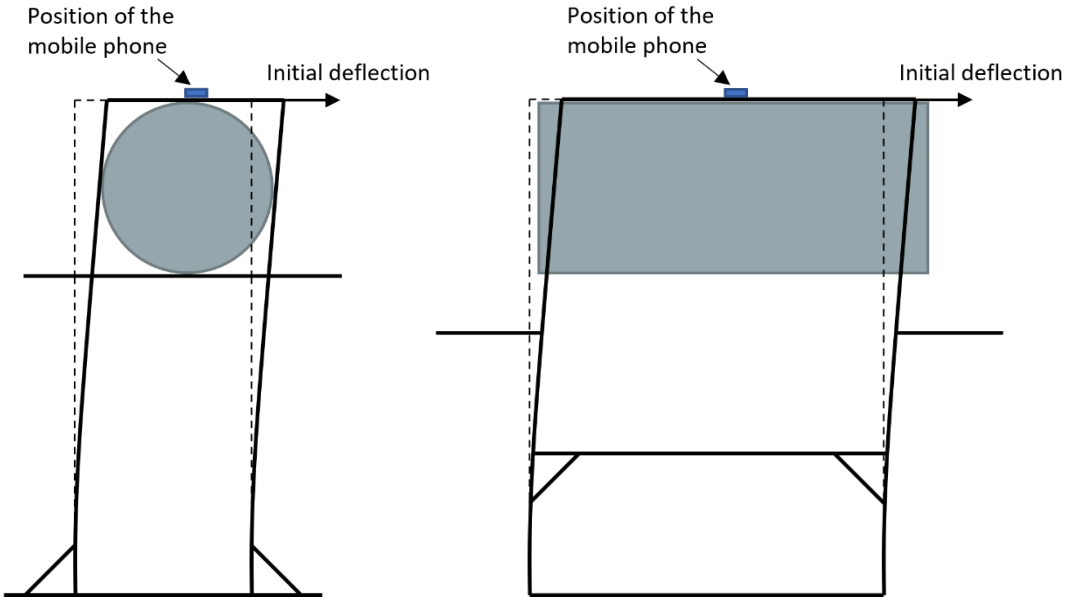

Figure 6 - The setup of the simple experiment to determine the natural frequencies of the construction.

The construction was deflected, and the acceleration was measured. Two measurements were conducted for deflections in each the X and Y direction.

The results of the experiment were transformed into a frequency domain and plotted to a graph (Figure 7). All the transformations and nontrivial calculations were done in MATLAB and the code can be found in electronic appendixes.

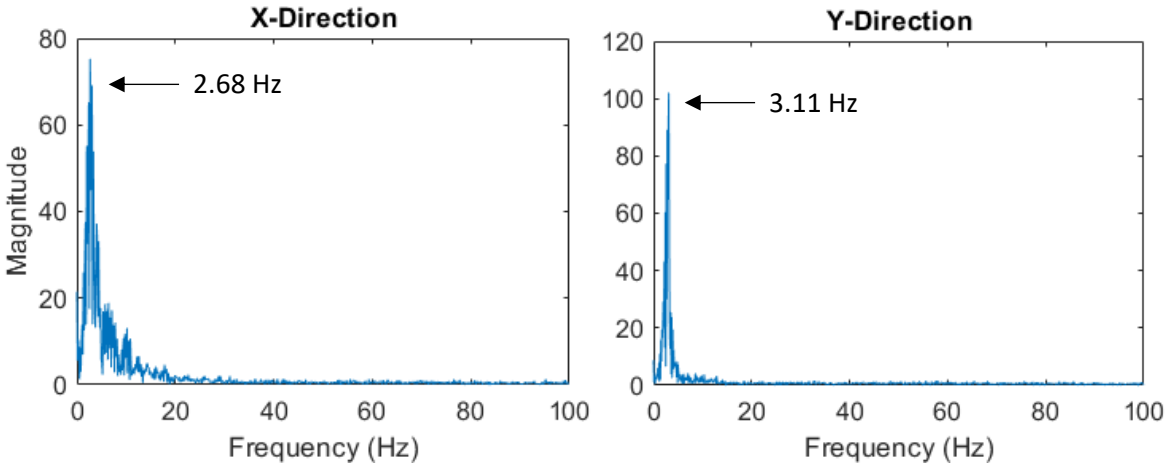

Figure 7 - The results of the experiment for determining the natural frequencies of the supporting construction.

3.3. Vacuum Pump

The minimal pressure that can be achieved in the vacuum chamber is10^{-4} Pa. This value is expected to be higher when a thruster is operating inside the vacuum chamber. Values close to 10^{-2} Pa are more realistic in those conditions. It is accomplished with two-stage pumping. The first stage pump is a rotary piston mechanical pump, and the second stage is a turbomolecular pump. Two rotary piston mechanical pumps and one turbomolecular pump are available at the facility. The parameters of the pumps are shown in Table 2. The table shows the parameters under the expected conditions.

Table 2 - Parameters of the vacuum pumps.

Model	Type	RPM	Volume flow rate	Achievable pressure
LAVAT VRO 4/11	Rotary piston mechanical	Not stated	4 m^3/hr.	5 Pa
TPH 240	Turbomolecular	60000	230 l/s (N_2)	10^{-2} Pa

3.4. Noise of the Environment

An experiment was carried out to determine the noise of the environment at the vacuum chamber. The goals of the experiment are the following:

- Determine the amplitude of the displacement caused by the noise of the environment
- Predict the possible impact of vibration isolation

3.4.1. Setup

A set of three Brüel & Kjær 14 g DeltaTron accelerometers was used for the experiment (the calibration chart is shown in Appendix 1. The data was obtained with an NI-9234 dynamic signal acquisition module.

The goal of the experiment was not to describe the modal parameters of the vacuum chamber, but rather to determine the conditions under which the thrust would be measured. That is why the chamber is left on the supports that would hold it during the thrust measurement.

The accelerometers were placed, so that they measure the acceleration in the X, Y, and Z direction. The coordinate system and the placement of the accelerometers are shown in Figure 8.

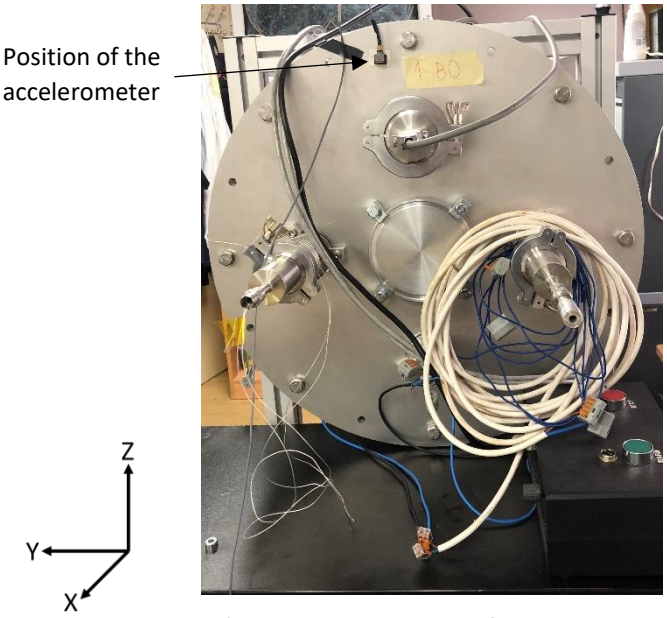

a) The accelerometer for the X direction.

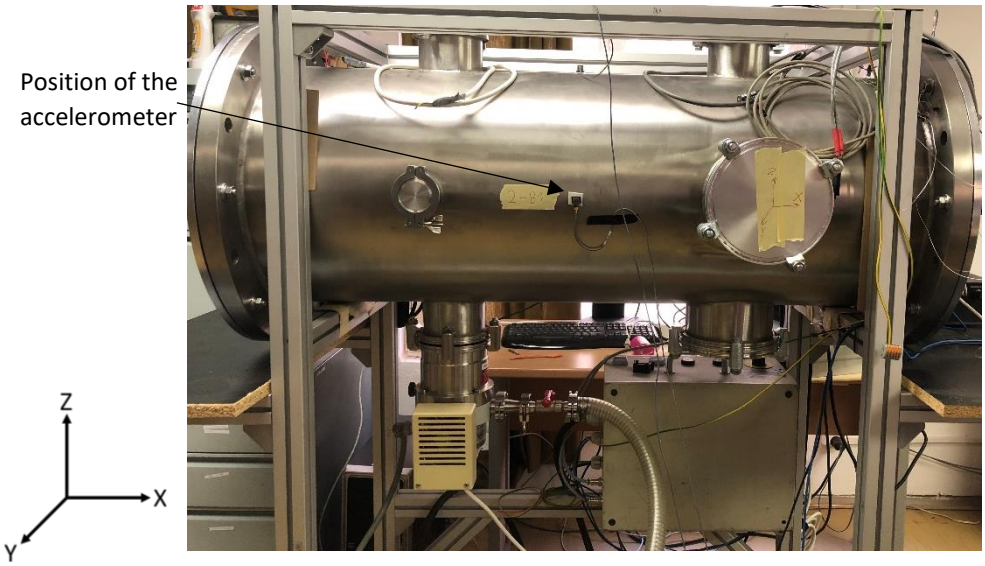

b) The accelerometer for the Y direction.

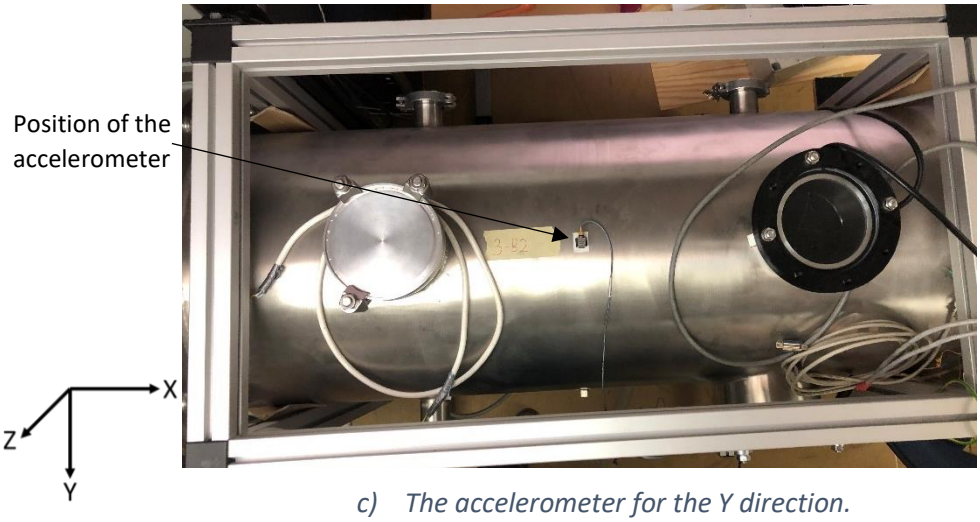

c) The accelerometer for the Y direction.

Figure 8 – The setup of the experiment to measure the noise of the environment.

3.4.2. Working Conditions

The measurement was carried out in five different working conditions, and at various frequencies. The description of individual setups is shown in Table 3.

Table 3 - Description of individual setups for the measurement of the noise of the environment.

Setup no.	Description
1	Only the rotary piston mechanical pump is running, and it is **right next** to the construction of the vacuum chamber.
2	Only the rotary piston mechanical pump is running, and it is **1.2 m** from the construction of the vacuum chamber.
3	Only the rotary piston mechanical pump is running, and it is **1.2 m** from the construction of the vacuum chamber. A foam underlay is added under the pump.
4	Like Setup 3 but the turbomolecular pump is running.
5	Only the turbomolecular pump is running.

The measured combinations of the setups and frequencies are shown in Table 4. The reason for measurements at these different combinations is that it enables the determination of the following:

- Which frequencies of the noise of the environment are caused by which element.
- By which portion each element contributes to the noise of the environment
- To what extend can the contribution of some elements be easily reduced
- Whether any of the frequencies could be caused by measurement inaccuracies.

Table 4 - The measured frequency ranges for each setup.

Setup no.	200 Hz	500 Hz	2000 Hz	4000 Hz
1	✓	✓	✓	×
2	✓	✓	✓	×
3	✓	×	×	×
4	✓	×	×	✓
5	×	×	×	✓

3.4.3. Evaluation

The output of the accelerometers (acceleration in time) was decomposed by fast Fourier transform (FFT). This transforms the data from the time domain into frequency domain allowing us to easily read the acceleration amplitude corresponding to each frequency. It should be noted that the relation between the magnitude in the FFT and the amplitude of the acceleration is:

$$A = \frac{2 \cdot M}{n}, \tag{2}$$

where A is the amplitude of the acceleration, M is the magnitude in the FFT, and n is the number of the samples.

The frequencies can be divided into 3 groups: frequencies associated with a specific element, frequencies independent of the setup (e.g., natural frequencies of the construction), and frequencies that are caused by measurement inaccuracies.

Comparison of setups 3 and 4 should identify frequencies of the turbomolecular pump, and the comparison of setups 4 and 5 the frequencies of the rotary piston pump. This is then verified by direct comparison of setups 1 and 5.

Special attention is focused on frequencies that are multiples of 50 Hz which is the frequency of a plug. Zero frequencies would mean a non-zero overall acceleration of the system. The system was observed during the measurement, and it was not the case, so those frequencies are not considered.

Individual setups were compared to obtain the frequencies corresponding to each element.

3.4.3.1. Identifying the Frequencies

Setups 1 and 5 were measured with no common element running. At setup 5, there were significant values at high frequencies. The measurements with the highest frequency ranges were compared. The comparison is shown at Figure 9.

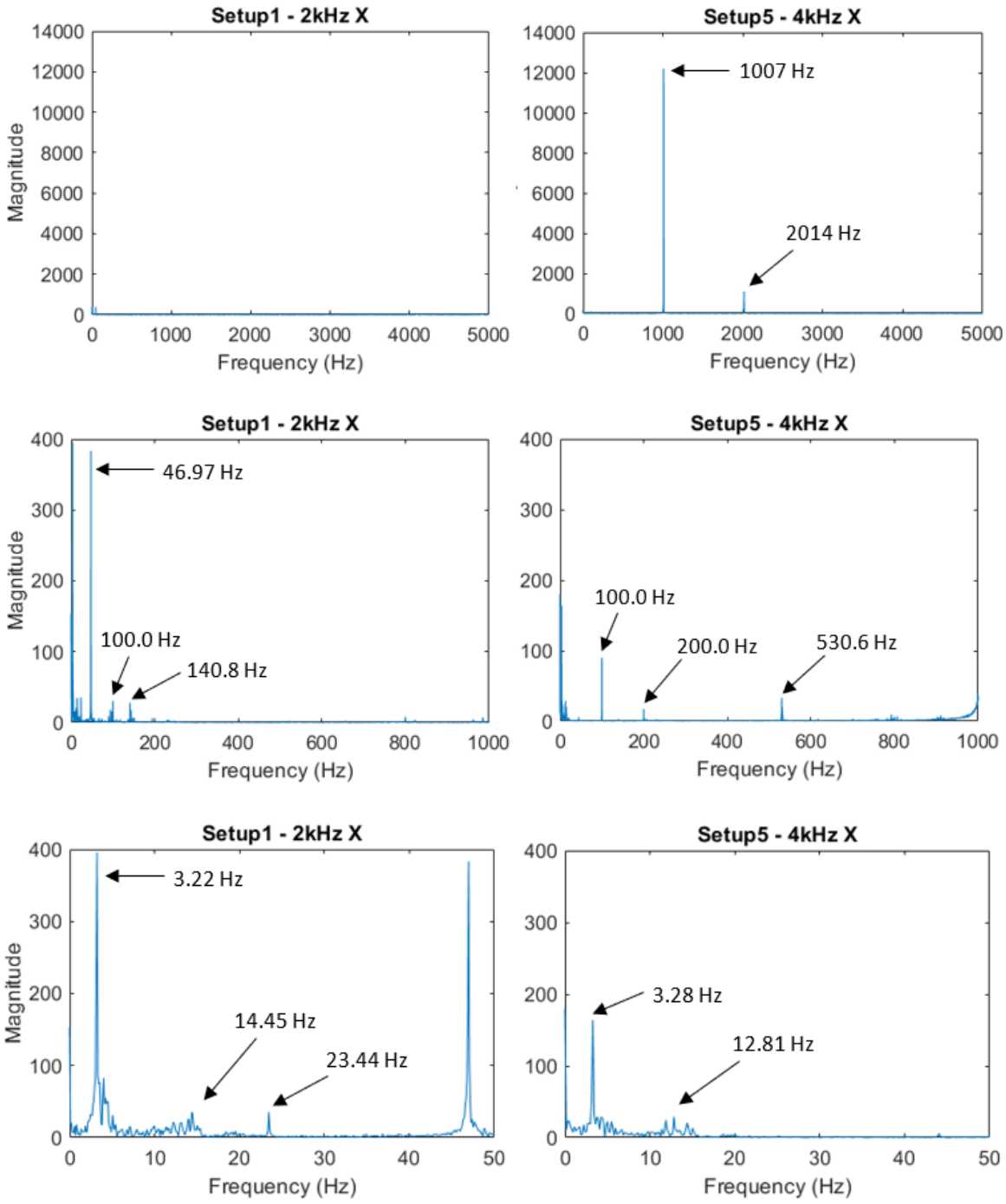

Figure 9 - The comparison of the results of the setups 1 and 5.

The peak at 1007 Hz and its multiples appear only when the turbomolecular pump is running and it is significant in all such measurements. It is also in accordance with the expected rpms of the pump. It is clear that this frequency is associated with the turbomolecular pump. In regard of the frequencies and amplitudes for individual directions of the setups 4 and 5, the frequency remains more or less constant (1007 Hz to 1009 Hz). The amplitude is significantly higher in the Y direction than in the X and Z directions.

When we zoom in, we can see a small peak at 530.6 Hz at setup 5. This frequency cannot be clearly assigned to the turbomolecular pump, because smaller peaks at similar frequencies also appear on the setups without it. It is assumed that this is one of the natural frequencies of the system and that it is only excited more significantly by the high frequencies of the turbomolecular pump.

The peaks at 100 Hz and 200 Hz are suspicious for two reasons. First, they are very precise multiples of the plug frequency (50 Hz) and second, the frequencies are more consistent across the directions and across the setups than any other frequency. On the other hand, mechanical isolation of a source of the vibrations (specifically the foam underlay under the rotary piston pump) clearly affects the magnitude at these frequencies. Moreover, the plug frequency itself does not have a significant peak (the closest is the peak at 47 – 48 Hz and it is only significant when the rotary piston pump is running). To be on the safe side, these peaks are, therefore, not ruled out.

The peak at 46.97 Hz is apparent on setup 1. Peaks at approx. 44 Hz are detectable in all directions of setup 5. These, however, are of much smaller magnitude, and are likely to be of different origin. Peaks at both 47-48 Hz and 44 Hz are detectable on setup 4, where both pumps are running (see Figure 10).

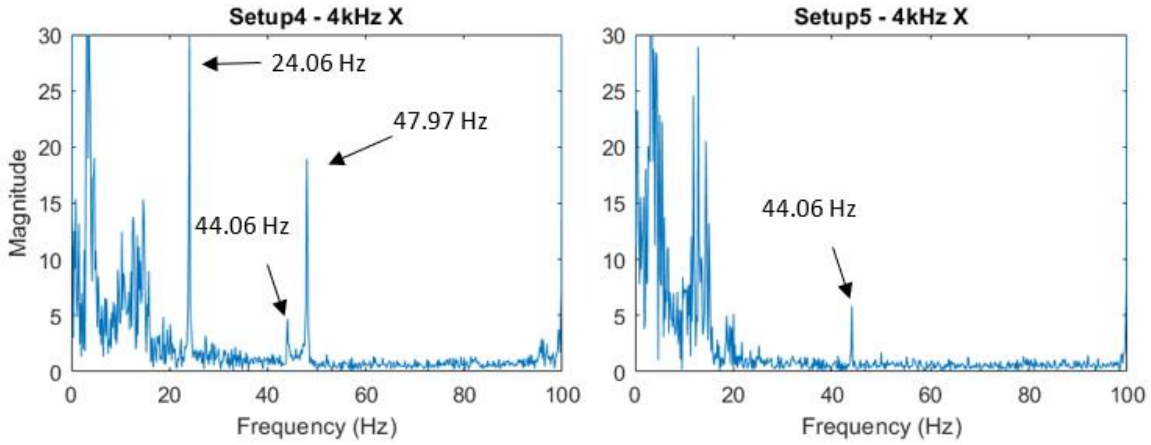

Figure 10 - The peaks at 44 Hz at setups 4 and 5.

Peaks at 23.5-24 Hz (half) also occur when the rotary piston pump is running and are higher in some directions and configurations (as can be seen on Figure 10). The manufacturer of the rotary piston pump does not state the rpms of the pump, but a value slightly lower than a fraction of the plug frequency would be reasonable for an asynchronous electro engine.

Between the frequencies 5 Hz and 15 Hz there is an apparent increase for almost all the setups. It is often dispersed with no sharp peak. The frequencies of the maximum value vary across the setups and directions.

The peak at 3.22 Hz is consistent irrespective of the setup and appears only in the X direction. In the Y direction, the peak appears at 3.9-4.4 Hz, and in the Z direction, there is no significant peak. This implies that these are the natural frequencies of the supporting

construction. The experiment in Chapter 3.2 supports this claim with the results in similar ranges. The frequencies in Chapter 3.2 were smaller in both directions. This is likely due to the fact that the amplitudes of deflection in Chapter 3.2 were substantially higher, which could lead to the effects of nonlinearity and damping to come forward.

No significant peak appears at lower frequencies. The low acceleration values at the lowest frequencies could still cause significant displacements since they act for a relatively long time. However, there is no known source of a noise at such frequencies. Moreover, the values show no consistency or any reasonable relation to the setup configuration.

3.4.3.2. Mechanical Isolation of the Rotary Piston Mechanical Pump

During the experiment, it was also tested, to what degree is it possible to easily isolate the rotary piston pump. The assumption was that the pump would be one of the main sources of the vibrations. The effect of two measures was tested. First, the pump was moved 1,2 m from the construction (setup 2). Second, a foam underlay was added under the pump (setup 3).

The results are summarized in Table 5.

Table 5 - The magnitudes of FFT in the frequency range of $200\ Hz$ in setups 1, 2, and 3 in each direction and the relative increase or decrease in relation to setup 1.

Frequency	Direction	Setup 1	Setup 2	Setup 3
$3.19 - 3.31$ Hz	X	3.15	5.66 (+80 %)	3.59 (+14 %)
$3.81 - 4.13$ Hz	Y	5.43	19.50 (+259 %)	10.77 (+ 98 %)
$9.38 - 10.75$ Hz	Z	9.71	7.07 (-27 %)	3.50 (-64 %)
$11.06 - 11.44$ Hz	Y	3.33	2.21 (-34 %)	1.20 (-64 %)
$11.94 - 14.38$ Hz	X	1.98	1.77 (-11 %)	1.08 (-45 %)
$23.81 - 24$ Hz	X	78.27	134.51 (+72 %)	53.13 (-32 %)
$23.81 - 24$ Hz	Y	7.41	12.86 (+74 %)	5.60 (-24 %)
$23.81 - 24$ Hz	Z	3.06	9.29 (+204 %)	4.19 (+37 %)
$47.63 - 48$ Hz	X	44.02	7.14 (-84 %)	2.82 (-94 %)
$47.63 - 48$ Hz	Y	38.74	4.25 (-89 %)	2.75 (-93 %)
$47.63 - 48$ Hz	Z	49.14	12.70 (-74 %)	7.28 (-85 %)
100 Hz	X	4.75	5.34 (-12 %)	0.44 (-91 %)
100 Hz	Y	19.72	10.17 (-52 %)	0.60 (-97 %)
100 Hz	Z	22.83	15.82 (-31 %)	1.14 (-95 %)
$195 - 200$ Hz	Y	8.67	4.02 (-54 %)	Insignificant

The results show that the effect of the isolation is inconclusive for lower frequencies (<30 Hz) and is significant at the higher frequencies.

3.4.4. Results

Figure 11 shows results from all the measurements summarized to a graph. Lines of equal displacement were added to better show the effect of vibrations on individual frequencies. Worst case scenario is assumed for the calculation of the displacements, which is a square wave. This leads to the following formula for calculating the amplitude of the displacement:

$$u_{amp} = \frac{a_{amp}}{16 \cdot f^2}, \tag{3}$$

where u_{amp} is the amplitude of the displacement, a_{amp} is the amplitude of acceleration and f is the respective frequency.

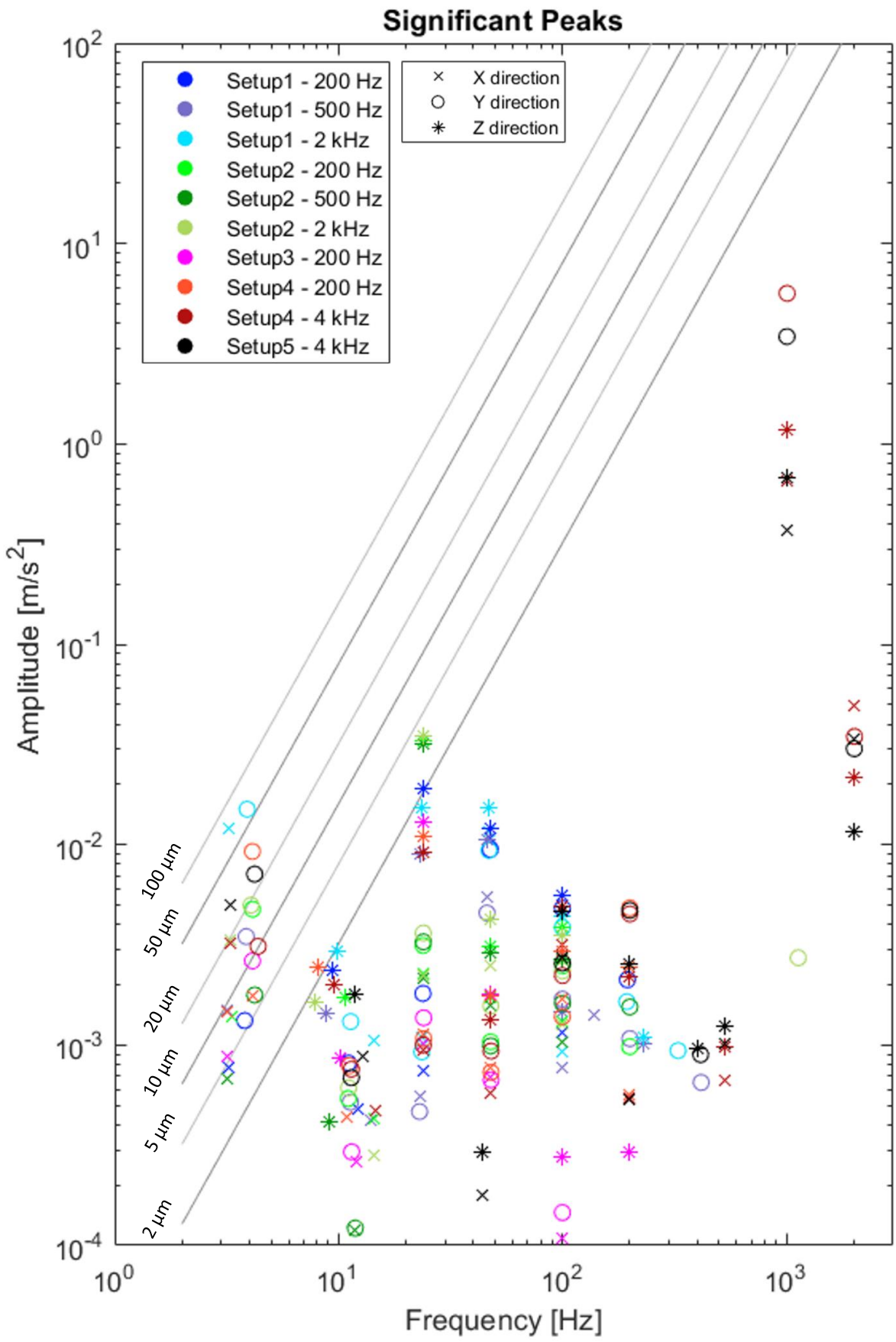

Figure 11 - The results of the measurement of the noise of the environment.

4. Choice of the Design Principle

In this chapter, the knowledge gained in chapters 2 and 3 is used to draft a possible design principle of the thrust stand. The parameters of individual components and their suitability for the working conditions is evaluated. The availability of the components is also taken into account.

4.1. Measurement principle

The task is to measure thrust, so the impulse bit measurement is not a good fit for this purpose. Measurement of the exhaust plume momentum was utilized in [6], and while it proved in our condition to be an effective method of thrust verification, it is fraught with too many uncertainties to be an effective method of measurement.

Direct thrust measurement offers high sensitivity and resolution making it a good fit for this application. The ability to fit into the relatively small vacuum chamber, and sensitivity to the noise of the environment were among the main factors to choose between the hanging pendulum, inverted pendulum, and torsional pendulum configurations.

Compactness is arguably the biggest strength of the inverted pendulum configuration [1]. It is stated in [1], that:

"Deflections of several millimeters are commonly achieved with pendulum lengths less than 20 cm, permitting use in vacuum chambers less than 1 m in diameter."

This implies that the spatial constraints would be a major challenge for our application since the diameter of the vacuum chamber is only 40 cm. On the other hand, the deflection does not necessarily need to be in the order of millimeters if high precision displacement sensors are used. The downside of this configuration is that it is very sensitive to the environment in general (specifically inclination). Given the inability to ensure a consistent inclination, an active inclination control system would first need to be designed for a successful use of the inverted pendulum configuration.

The main advantage of the torsional pendulum configuration is the ability to accommodate either thrusters with changing mass or very large range of thruster weights. Although this is undoubtedly a benefit, it is not one of the objectives of this thesis. This configuration also has high sensitivity and less environmental noise sensitivity than inverted pendulums.

To achieve the high sensitivity, the torsional pendulums require long arms and are thus hard to accommodate in smaller vacuum chambers. The torsional pendulums are often complex which in our particular conditions is not outweighed by the independency on the thruster mass.

The hanging pendulum can be relatively simple and easy to use. Also, their susceptibility to changes in flexure stiffness and inclination is low. For this reason, the hanging pendulum was chosen as a concept for our thrust stand.

The hanging pendulums require either a long arm or a high precision displacement sensor to measure thrusters with low thrust-to-weight ratio. A high precision displacement sensor is available at the facility (more details are provided in chapter 5.2.7), but the amplitude of the deflection caused by the environmental noise exceeds the precision of the sensor. Therefore, a vibration isolation system might be necessary. Vertical orientation of the vacuum chamber would allow the length of the pendulum arms to be 600 mm or more.

4.2. Components

Suitability for our conditions of certain types of individual components is compared and the specific types are selected.

4.2.1. Pendulum Arms

The sensitivity of a hanging pendulum thrust stand can be characterized by a static balance of the pendulum arms. The simplest form of a hanging pendulum trust stand with a counterweight is shown on Figure 12.

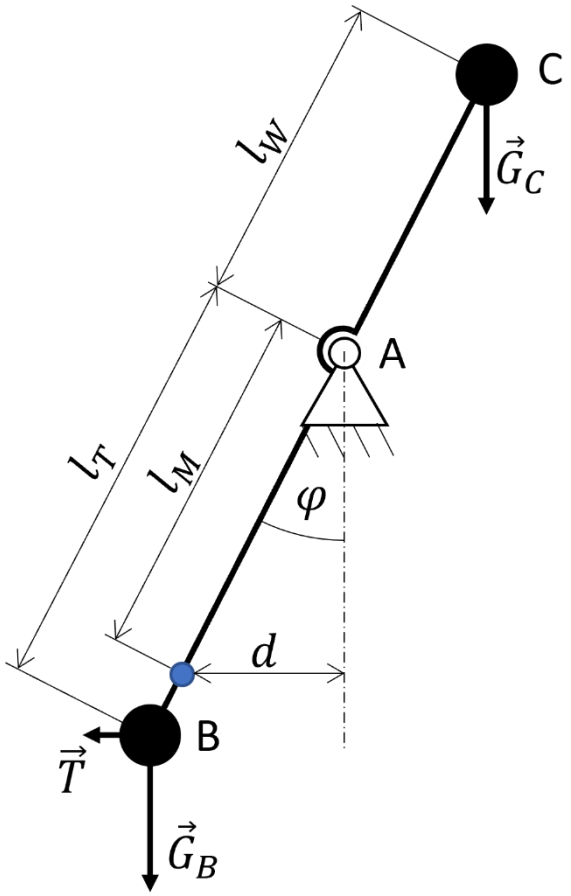

Figure 12 – A diagram of a hanging pendulum with a counterweight.

From the static analysis, the deflection can be calculated as:

$$d = l_M \cdot \sin\left(atan\left(\frac{T \cdot l_T}{G_B \cdot l_T - G_C \cdot l_W}\right)\right), \tag{4}$$

where d is the deflection, l_T, l_W and l_M are the respective distances from the pivot to the thruster, counterweight, and the point of deflection measurement, T is the thrust and G_B and G_C are the respective weights of the thruster and the counterweight. The thruster is simplified into a mass point so the possible offset of the origin of the thrust from the center of gravity of the thruster is neglected. For small angular deflections, the equation can be simplified to:

$$d \approx l_M \cdot \frac{T \cdot l_T}{G_B \cdot l_T - G_C \cdot l_W}. \tag{5}$$

Using multiple parallel pendulum arms can make the thrust stand independent of the position of the center of mass of the thruster (in rigid body mechanics). An example of such configuration is shown in Figure 13.

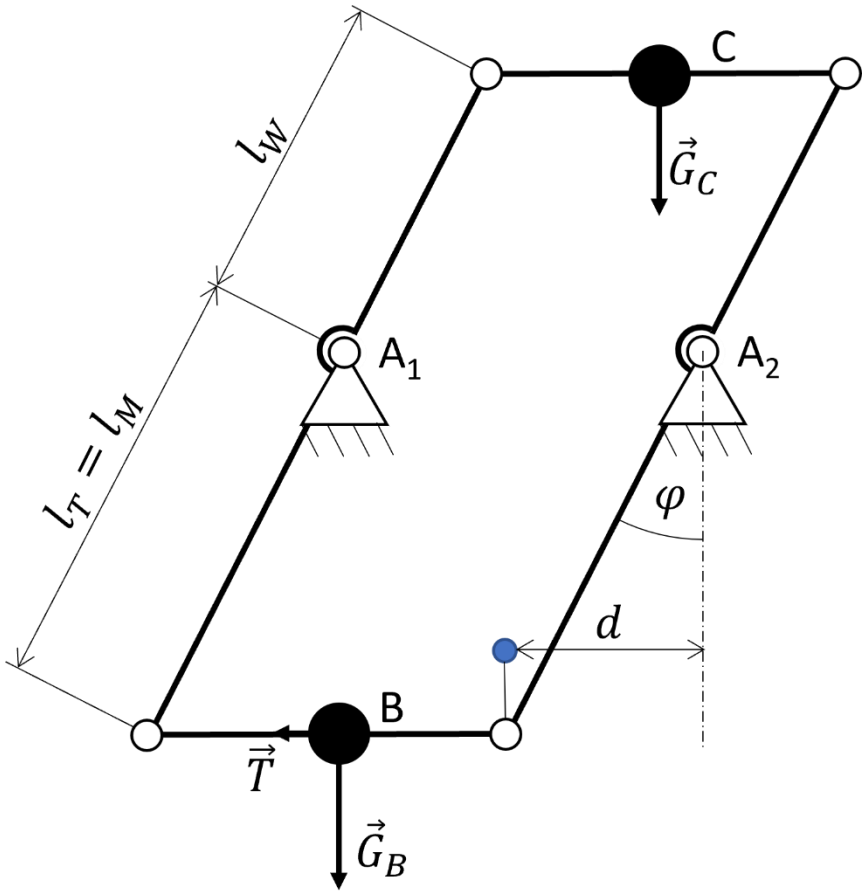

Figure 13 - A configuration of a hanging pendulum with parallel pendulum arms.

In this case it is apparent a horizontal shift of the mass point does not change the distribution of the forces. While a vertical shift does change the distribution of the forces, the resultant angle φ remains the same. If the point of measurement is connected to the platform as in Figure 13, then $l_M = l_T$. The formula can thus be simplified to:

$$d = \frac{T \cdot l_T^2}{G_B \cdot l_T - G_C \cdot l_W}. \quad (6)$$

The sensitivity can then be easily calculated as:

$$s = \frac{d}{T} = \frac{l_T^2}{G_B \cdot l_T - G_C \cdot l_W}. \quad (7)$$

This principle also applies in 3D for 4 parallel arms.

A configuration with 4 parallel arms was chosen for our thrust stand.

4.2.2. Spring Element

A torsional spring acting to increase the deflection was considered. However, with the chosen configuration it could lead to instability. Also, since the stand already uses a counterweight to act against the restoring forces, it was decided not to combine multiple approaches so that the uncertainties are not increased unnecessarily.

The purpose of the pivot is to allow rotational movement with the least possible resistance. Therefore, a knife edge mechanism is used for each revolute joint. A specific formula for the resistance of such mechanisms was not found in the literature, but it is generally agreed, that the effect of using the knife edges results in minimization of the resistance [19] [20]. A similar concept was introduced in [21], where two crossover knife edges were used to also allow the measurement of the forces in the transversal direction. Typical materials for knife edges are hard materials such as tungsten-carbide, cubic boron nitride, sapphire, or diamond [19] [20].

4.2.3. Displacement sensor

A high precision displacement sensor Micro-Epsilon ILD1420-50 is available at the facility. It works on a principle of laser triangulation. The key properties of the sensor are shown in Table 6.

Table 6 - The key parameters of the displacement sensor.

Start of measuring range	End of measuring range	Repeatability
35 mm	85 mm	2 µm

Since the accuracy of the sensor is very high (the noise of the environment is larger than the repeatability of the sensor), and the attachment of the sensor has already been solved in [6], no other sensors had to be considered for the thrust stand.

4.2.4. Damper

As the resistance of the joints is minimized, the system needs a separate damper so that it does not oscillate around the balanced position. Since the dynamic behavior of the thrust stand is not a point of our interest, there is no need for any specific damping constant. Overdamped system might be advantageous because it eliminates the risk of excitation of its natural frequencies.

Eddy current damper was chosen for this purpose because it is simple and effective. The damper is placed on the upper platform. This brings several benefits. The weight of the

damper does not decrease the thrust-to weight ratio of the thruster. Also, the magnetic field of the damper does not interact with the magnetic field of the thruster.

4.2.5. Vibration Isolation

Since the precision of the used displacement sensor is very high, decreasing the noise of the environment leads to an increase of the accuracy of the measurement. The isolation can be either placed inside the chamber or outside.

Since the most significant noise is at the natural frequencies of the supporting construction, placing the isolation outside seems like a logical option. Increasing the stiffness of the construction should lead to an increase of the natural frequencies and thus the decrease of the amplitudes with very little effort. A damping element either under the construction or between the construction and the chamber could isolate the chamber from external sources of noise. However, there are also internal sources of noise (the turbomolecular pump and its cooling mechanism) so an isolation inside the chamber might also be needed. The effect of the stiffness increase should be verified by another measurement of the noise of the environment. It should also be noted that the chamber was in a horizontal position during the original measurement and a change to a vertical position also affects the natural frequency of the system because it shifts the center of mass significantly.

4.3. Calibration

Calibration of the thrust stand is accomplished by application of known forces on the lower platform. An often-used method to apply known forces is by using a pulley system to load known weights [1]. However, the forces applied this way were larger by more than one order of magnitude than in our case.

Known forces in the order of 10^{-5} N or lower can be applied using an electrostatic field [22], so this concept was chosen for the calibration of the thrust stand.

5. Preliminary Design

In this chapter, the design principles from chapter 3 are put together to create a preliminary design of the thrust stand. Forms of resistance and uncertainties of the thrust stand are explored and ways to eliminate or reduce them are discussed.

5.1. Iteration Zero

Only the pendulum arms, pivots and the platforms were considered in this iteration. The goal of this iteration is to determine the main properties of the thrust stand.

5.1.1. Position

After consultations with the supervisor of this thesis it was determined that the optimal placement of the thruster is that when the exhaust plumes are aimed directly towards the turbomolecular pump. This is because the air in the vacuum chamber can no longer be considered a continuum and the pump relies on a statistical probability of the air molecules to reach it. The probability of the molecules reaching the pump is evidently increased by aiming the exhaust plumes towards it.

The displacement sensor can be placed at the opening opposed to the pump, which is also a benefit of this placement. The position is $250\ \mathrm{mm}$ above the base of the chamber.

5.1.2. Design

For this iteration only the thrust stand itself was designed and only simplified representations of the components were used. The thruster being $250\ \mathrm{mm}$ above the base of the chamber leaves $750\ \mathrm{mm}$ above the thruster. The length of the arms was selected as $600\ \mathrm{mm}$. This leaves space for the upper platform with counterweight and potential elongation of the arms, if necessary. The pivots are parts of the pendulum arms in this iteration. The platforms are represented as simple blocks. The model is shown in Figure 14.

Figure 14 - The CAD model of iteration zero.

5.1.3. Calculations

The mass of the measured thruster is expected to be in the order of 0.2 kg. The mass of the bottom section is concentrated to a mass point which is positioned to the center of the platform and is set to 0.5 kg (the position of the point is irrelevant as mentioned in chapter 4.2.1). The mass point includes the mass of the thruster, the bottom platform, the calibration instrument, the pivots, and parts of the pendulum arms. The mass of the counterweight is set according to the expected uncertainties in determining the lengths, the mass of the bottom section, and the mass of the rest of the upper section. The upper limit of the mass is

$$m_{Cmax} = m_B \cdot \frac{l_T}{l_W}, \tag{8}$$

in which case the system is in neutral equilibrium. From (), the closer m_C is to m_{Cmax}, the higher is the sensitivity of the thrust stand. However, if the values are too close, there is a risk of instability due to the uncertainties. A margin of 5 % was chosen, which should give a sufficient sensitivity and should not be at risk of instability.

The sensitivity of the thrust stand was calculated according to (). The dependency of the sensitivity to the $\frac{l_T}{l_W}$ ratios was calculated and plotted to a graph (Figure 15).

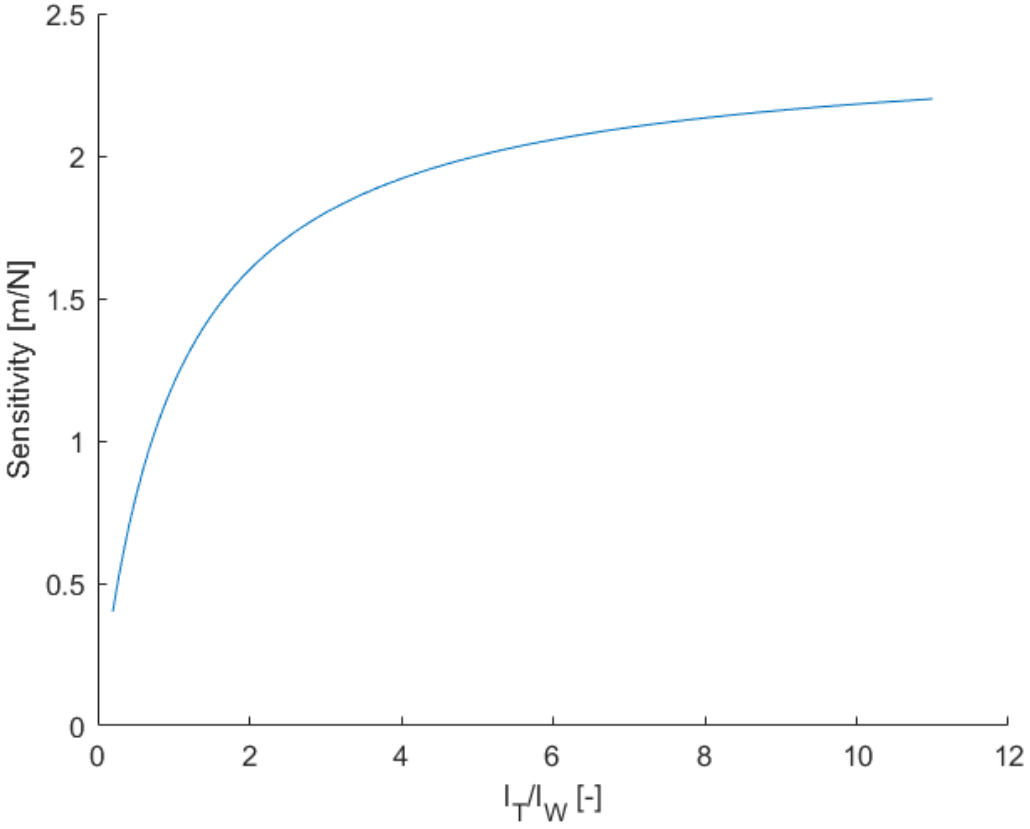

Figure 15 - The sensitivity in relation to the $\frac{l_T}{l_W}$ ratio.

The changed sensitivity caused by an inaccurate determination of the mass of the bottom section by 1 % was plotted to a graph (Figure 16).

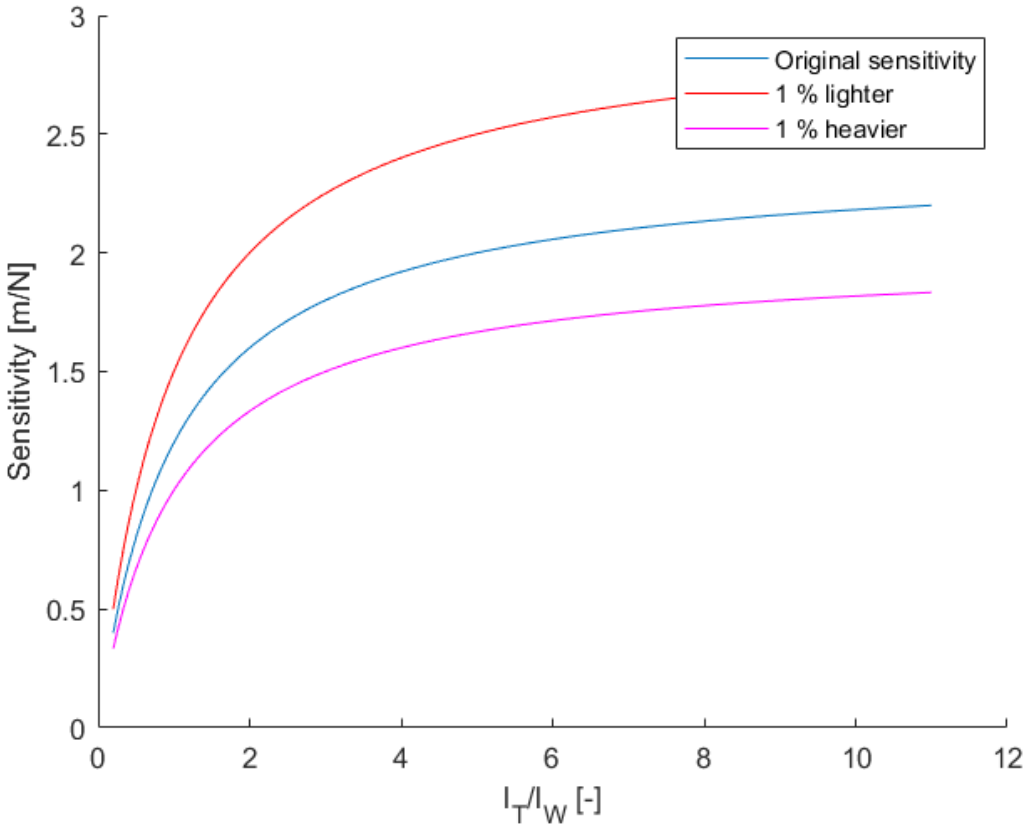

Figure 16 - The changed sensitivity caused by a 1 % change in mass.

The advantage of a high $\frac{l_T}{l_W}$ ratio is clearly a higher sensitivity. However, since the $\frac{l_T}{l_W}$ is proportional to the ratio of the masses and the mass of the bottom section is fixed, a higher $\frac{l_T}{l_W}$ ratio implies higher overall mass which increases the load on the pivots. The ratio is selected as $\frac{l_T}{l_W} = 2$. A further increase of the ratio does not lead to a significant increase in the sensitivity. The parameters of the stand are $l_T = 400\ \text{mm}$, $l_W = 200\ \text{mm}$, $m_C = 0.95\ \text{kg}$,
$s = 1.630\ \text{mm} \cdot \text{N}^{-1}$. The displacements under maximal thrust $T_{max} = 2\ \text{mN}$ are $\varphi_{max} = 8.2\ \text{mrad}$ and $d_{max} = 3.26\ \text{mm}$. The ratio may be changed further on, as the inaccuracies caused by a higher load on the pivot are inspected.

The natural frequency of the system is calculated from the equation of motion. For an undamped system:

$$I_{Yp} \cdot \ddot{\varphi} + k_{ef} \cdot \varphi = 0, \tag{9}$$

where I_{Yp} is the moment of inertia to the Y axis passing through the pivots center of the base platform and k_{ef} is an effective stiffness of the system (a moment response to a unit angular displacement). For the simplified system the moment of inertia and the effective stiffness can be calculated as:

$$I_{Yp} = m_B \cdot l_T^2 + m_C \cdot l_W^2 \tag{10}$$

And

$$k_{ef} = m_B \cdot l_T \cdot g - m_C \cdot l_W \cdot g. \tag{11}$$

The natural frequency can be calculated as:

$$\Omega = \sqrt{\frac{k_{ef}}{I_{Yp}}} \tag{12}$$

$$\Omega = 0.921 \text{ rad} \cdot \text{s}^{-1} = 0.147 \text{ Hz}$$

5.1.4. NX Motion Simulation

The behavior of the system was simulated in NX Motion to verify the calculations and to allow us to determine other properties of the system. NX Motion is an engineering software used to simulate multibody dynamics to engineer performance for moving mechanisms. For our simulation, we considered all parts to be rigid bodies. An assumption of the pivots is that they allow only one rotary motion, in our case around the Y axis. This implies that no relative motion is happening between the two pendulum arms that rotate around the same axis. Those were, therefore, put into the simulation model as one body. The system can be simplified to a 2D problem with four links representing two platforms and two pairs of pendulum arms (Figure 17).

Figure 17 - The simplification for the NX Motion simulation.

The configuration contains 6 pairs of pivots with each pair belonging to the same body. NX Motion offers various joint definitions. The revolute joint restricts all degrees of freedom but one rotation. Even though using a revolute joint, each for one pair of pivots, leads to restricting the same degrees of freedom multiple times, the software can

automatically remove the redundant constraints. Since the constraints are not conflicting, this does not lead to unexpected behavior of the system. The respective mass properties were assigned to the links representing the platforms. The system was loaded by gravity and by a force of 10^{-5} N in the X direction representing the thrust (the value is 10% of the minimal expected thrust and was selected as a sufficient accuracy).

The duration of the simulation is set to 20 s to comfortably include a full period of the motion. A marker was added to the bottom platform to track the displacement, because this is where the displacement would be measured in reality. The results of the simulation are shown in Figure 18. The period of the motion from the simulation is $T = 6.824$ s. The natural frequency is $\Omega_{Hz} = \frac{1}{T} = 0.147$ Hz, which is in accordance with the calculations. The mean value of deflection is slightly above 0.016 mm (which would correspond to the sensitivity of $1.630\ \mathrm{m} \cdot \mathrm{N}^{-1}$).

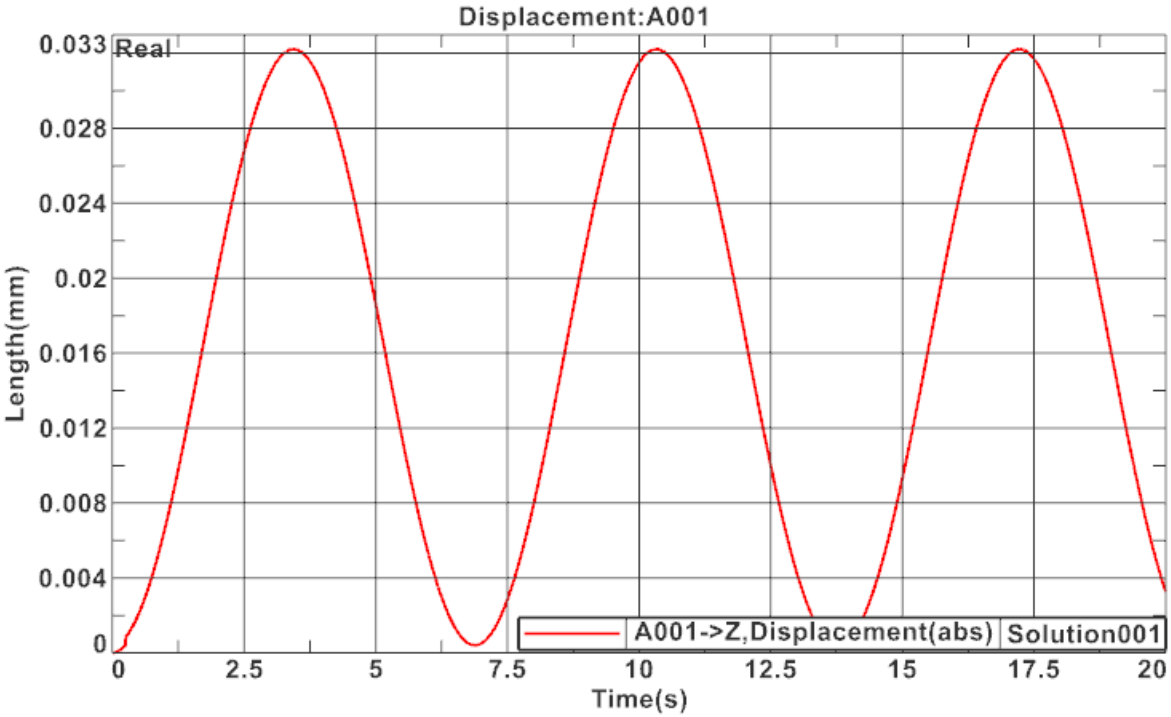

Figure 18 - Results of the NX motion simulation without damping.

A damper was attached to the upper platform to get a more accurate value for the sensitivity. The damping constant was varied iteratively to achieve a fast convergence toward a steady state. The resulting damping constant was $5\ \mathrm{kg} \cdot \mathrm{s}$. The behavior of the damped system is shown in Figure 19.

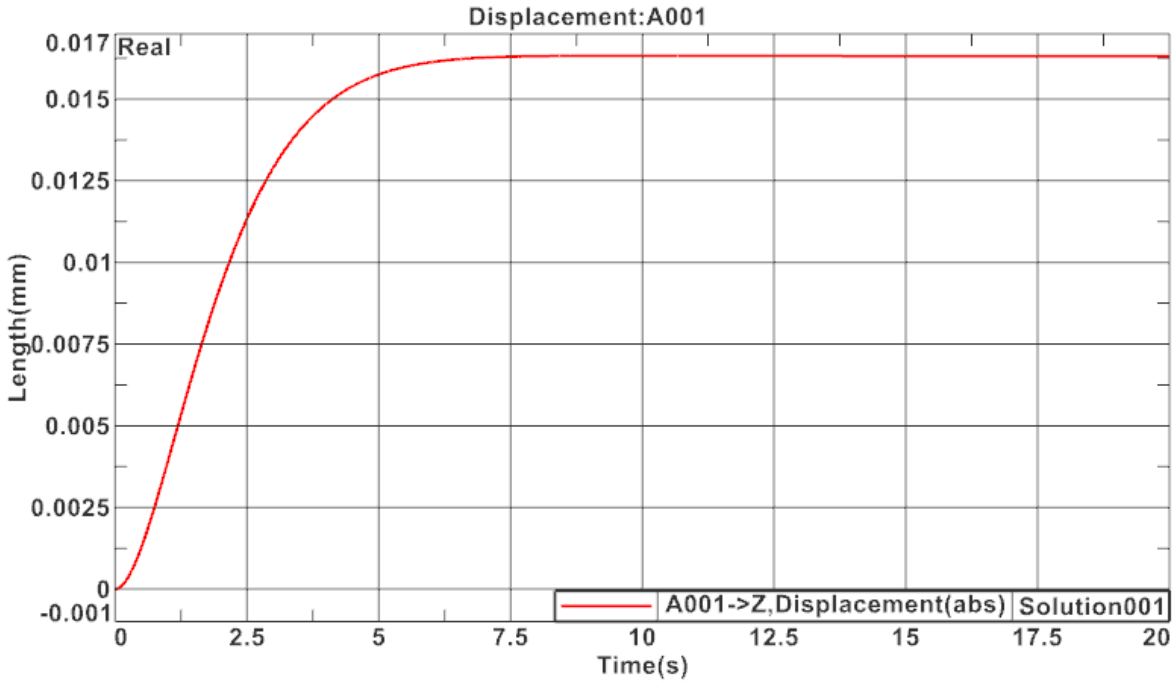

Figure 19 - The results of the NX Motion simulation with a $5\ kg \cdot s^{-1}$ damper connected to the top platform.

The value of the displacement converges to $0.01632\ \mathrm{mm}$ so the measured sensitivity is $1.632\ \mathrm{m} \cdot\ \mathrm{N}^{-1}$ which is slightly higher than the calculated value. The difference is small and is likely due to the different value of gravitational acceleration used. NX Motion uses the conventional standard value while in the calculations, the value corresponding to Prague was used (the value corresponding to Prague is more relevant for us since all the measurements would take place there).

5.2. Iteration One

Iteration zero gave a general understanding of how the thrust stand would look like and how would it behave. In iteration one the focus is on the concrete design of individual components, analysis of the parasitic forces associated with each component and reduction of these forces.

5.2.1. Pendulum Arms

For manufacturing, it is much more convenient to have pendulum arms and pivots as separate components. This also allows altering the $\frac{l_T}{l_W}$ ratio, and/or changing the length of the pendulum arms. Contradicting properties must be balanced for optimal performance. The requirements for the pendulum arms are sufficient stiffness to resist significant deformation and buckling on one hand, and on the other hand low mass and high compliance to decrease the resistance caused by a difference in the lengths of the pendulum arms. The origin of this resistance is shown in Figure 20Figure 19.

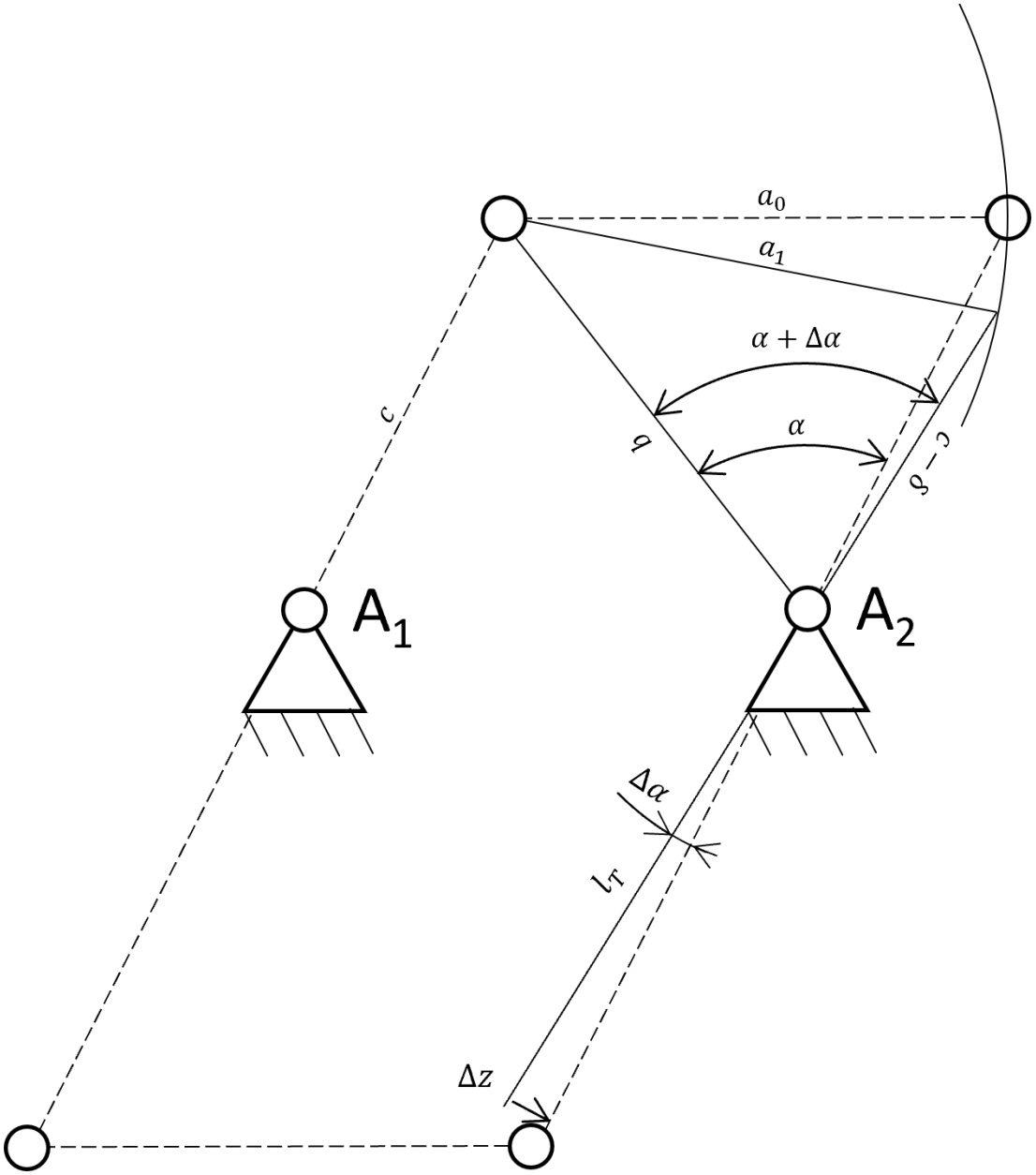

Figure 20 - The origin of additional resistance with pendulum arms of unequal lengths.

In this specific case, the length l_W of one pendulum arm is shorter by δ. For clarity, the figure shows a theoretical situation, where the bottom platform is not connected, so the pendulum arms can rotate into a non-parallel state. The length of the upper platform remains unchanged, so $a_0 = a_1$. The angles α and $\alpha + \Delta\alpha$ can be calculated from the law of cosines as:

$$\alpha + \Delta\alpha = \arccos\left(\frac{b^2 + (c-\delta)^2 - a_1^2}{2 \cdot b \cdot (c-\delta)}\right), \tag{13}$$

And

$$\alpha = \arccos\left(\frac{b^2 + c^2 - a_0^2}{2 \cdot b \cdot c}\right), \tag{14}$$

where b is a function of φ. It can be calculated also from the law of cosines as:

$$b = \sqrt{|A_1A_2|^2 + c^2 - 2 \cdot |A_1A_2| \cdot c \cdot \cos\left(\frac{\pi}{2} - \varphi\right)}. \quad (15)$$

In reality, the bottom platform resists the change of the angle, and the pendulum arm bends. The displacement needed to bend the pendulum arm at the bottom end of the pendulum arm can be calculated as:

$$\Delta z = 2 \cdot l_T \cdot \sin\left(\frac{\Delta\alpha}{2}\right). \quad (16)$$

We can assume, that this displacement is equally distributed between the pendulum arms. The force necessary for this displacement can be calculated using an influence coefficient:

$$F_Z = \frac{\Delta z}{2} \cdot \frac{3 \cdot E \cdot 2 \cdot J_Z}{l_T^2 \cdot (l_T + l_W)}, \quad (17)$$

where J_Z is the second moment of area about the Z-axis, and E is the elastic modulus of the material.

This force F_Z arises from the comparison of the states:

- The pendulum arms are of equal length. The angular deflection is φ.
- One of the pendulum arms is shorter by δ. The angular deflection is φ.

This, however, neglects the fact that for zero thrust, the pendulum arms would not be parallel if one was shorter by δ. The relative angle $\Delta\alpha_0$ would cause an internal force F_{Z0} for zero thrust. A necessary initial condition is that for zero thrust there are no internal forces. A correction is introduced to fulfill this condition, that $\Delta\alpha^* = \Delta\alpha - \Delta\alpha_0$.

The corrected values Δz^* and ΔF_Z^* are then calculated as:

$$\Delta z^* = 2 \cdot l_T \cdot \sin\left(\frac{\Delta\alpha^*}{2}\right), \quad (18)$$

and

$$F_Z^* = \frac{\Delta z^*}{2} \cdot \frac{3 \cdot E \cdot 2 \cdot J_Z}{l_T^2 \cdot (l_T + l_W)}, \quad (19)$$

The force on the upper platform is from the law of the lever $F_{ZC}^* = F_Z^* \cdot \frac{l_W}{l_T}$. These forces influence the angular displacement φ. This in turn influences the values of $\Delta\alpha$ and b, and therefore, also Δz and F_Z. The angular displacement with respect to this parasitic force can be calculated as:

$$\varphi_1' = \frac{T \cdot l_T - F_Z^* \cdot (2 \cdot l_T - l_W)}{G_2 \cdot l_T - G_3 \cdot l_W}. \quad (20)$$

Expressing the angular displacement directly from thrust would lead to unnecessarily complicated equations, since they can be easily solved iteratively with sufficient accuracy.

The solution largely depends on the bending stiffness of the pendulum arms $E \cdot J_Z$. The minimal value of the stiffness is calculated from the buckling condition. Only the upper parts of the pendulum arms were inspected since the bottom parts are tension. The nature of the inspected buckling is shown in Figure 21.

Figure 21 - The nature of the buckling at risk.

This type of buckling is described by the equation:

$$F_{cr} = \frac{\pi^2 \cdot E \cdot J}{l^2}. \tag{21}$$

In our case, the equation is:

$$F_{cr} = \frac{\pi^2 \cdot E \cdot J_Z}{l_W^2}, \tag{22}$$

where F_{cr} is the critical force, where the buckling occurs. For 4 pendulum arms we can express the minimal bending stiffness as:

$$(E \cdot J_Z)_{min} = \frac{k \cdot \frac{G_C}{4} \cdot l_W^2}{\pi^2} \tag{23}$$

$$(E \cdot J_Z)_{min} = 37\,785\ \mathrm{N \cdot mm^2}.$$

This value is very small (for example a Dural rod with a 2x2 square intersection would have the bending stiffness $E \cdot J_Z = 96\,000\ \mathrm{N \cdot mm^2}$). Therefore, the intersection and the material of the pendulum arms can be designed without considering buckling. The intersection was designed as a $3\ \mathrm{mm}$ x $6\ \mathrm{mm}$ rectangle for the Y and Z axes respectively. The quadratic moment of area of a rectangle can be calculated as:

$$J_Z = \frac{1}{12} \cdot b \cdot h^3 \tag{24}$$

$$J_Z = 13.5\ \mathrm{mm^4}.$$

The material selected for the pendulum arm was Dural. The elastic modulus of Dural is approximately $E = 72\,000\ \mathrm{N \cdot mm^{-2}}$ (depending on the specific type of Dural). With the properties of the pendulum arms introduced, the influence of the unequal lengths of the pendulum arms can be further examined.

The linearity of the system is still almost perfect so the sensitivity can be expressed as a function of only δ (and not T). The relation is shown in Figure 22.

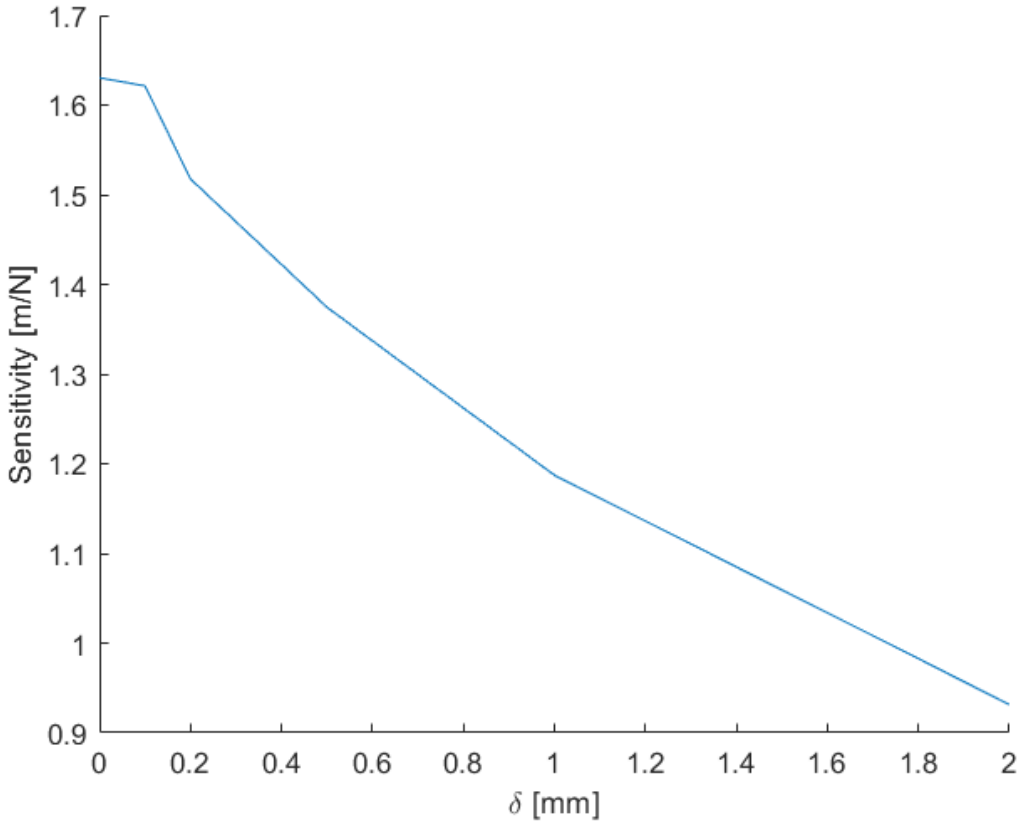

Figure 22 - The relation of sensitivity on δ.

Separate rods with highly precise lengths can be used to decrease the inaccuracies in the lengths of the pendulum arms. However, the final precision of the lengths l_T and l_W is hard to estimate and would have to be tested.

5.2.2. Pivot

Since no relative motion is happening between the two pendulum arms that rotate around the same axis, the corresponding pivots can be attached to each other mechanically. This would add a little weight to the system, but it would also simplify the assembly of the thrust stand.

Tungsten-carbide was chosen as the material for the knife edges as it was proven to be a well performing material in [19]. The resistance of a knife edge pivot is equal to the rolling resistance of the edge. In [19], the torque caused by the hysteresis of a tungsten-carbide knife edge was examined. The knife edge showed no significant hysteresis when

rotated less than $8\ \mathrm{mrad}$ under a $700\ \mathrm{N}$ load. The contact area was $100\ \mathrm{mm}$ by $5\ \mu\mathrm{m}$. Since the thrust stand would be rotated only slightly over $8\ \mathrm{mrad}$ in an ideal situation, and the maximal load would not exceed $20\ \mathrm{N}$, a significantly smaller area may be used still without encountering hysteresis. A $10\ \mathrm{mm}$ by $5\ \mu\mathrm{m}$ area was chosen for each knife edge resulting in a $40\ \mathrm{mm}$ by $5\ \mu\mathrm{m}$ overall supporting area. Even though the hysteresis does not occur under the working circumstances, the knife edge is a delicate part and must be treated accordingly.

5.2.3. Thruster Platform

The thruster platform needs an interface to connect the thruster and four flats to connect with the knife edges. The faces of the flats are slightly curved so that the placement of the knife edges is more repeatable. The interface should be easily accessible to allow easy attachment of the thruster. Behind the thruster, there should be space, so that nothing interferes with the outcoming exhaust fumes.

Low weight is a key parameter of the thruster platform. First, the platform was sub optimally designed to fulfill the necessary requirements (Figure 23).

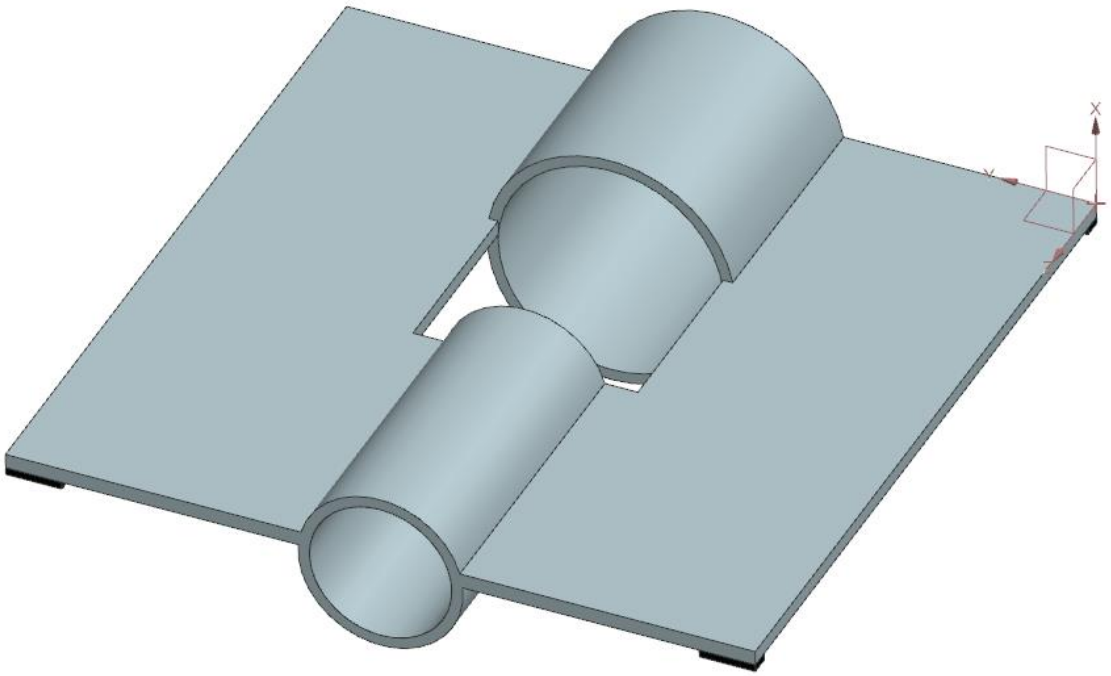

Figure 23 - The suboptimal thruster platform.

The mass of the suboptimal part is $0.516\ \mathrm{kg}$. A topology optimization was run to design an optimal, light platform. ANSYS was used for the topology optimization. A topology optimization is an iterative finite element method simulation where the goal is to remove unnecessary mass from an object based on some defined criteria. First, a mesh was defined for the model. The settings of the mesh were adjusted so that there are at least two elements through each wall, but at the same time the number of elements is not higher

than necessary (the computational cost of topology optimization is high). The settings and the resultant mesh are shown in Figure 24.

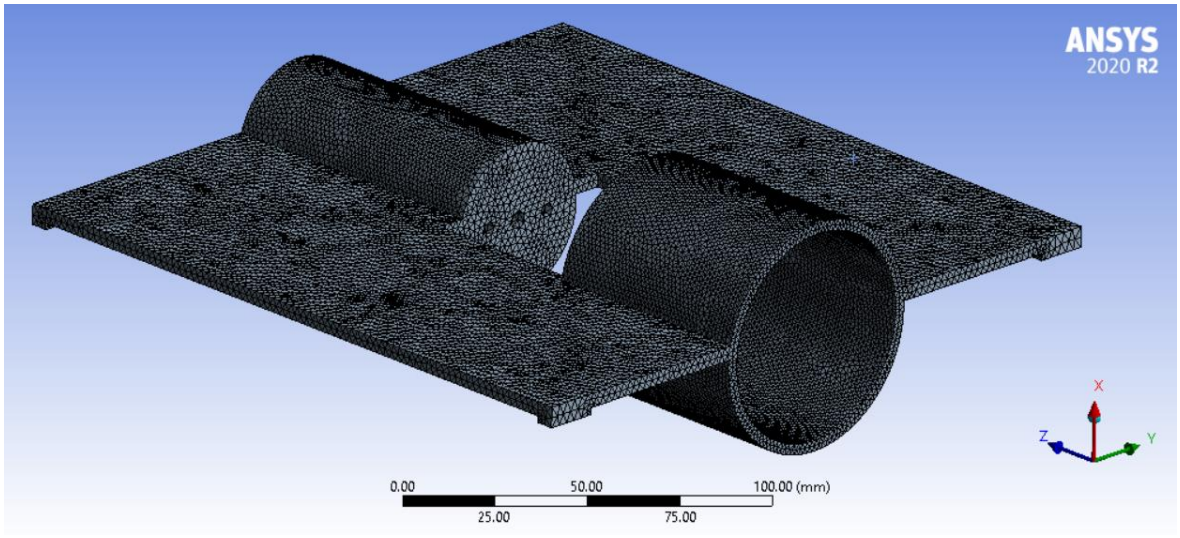

a) The mesh

Details of "Mesh"	
Display	
Display Style	Use Geometry Setting
Defaults	
Physics Preference	Mechanical
Element Order	Program Controlled
Element Size	Default (14.523 mm)
Sizing	
Use Adaptive Sizing	No
Growth Rate	Default (1.85)
Max Size	Default (29.047 mm)
Mesh Defeaturing	Yes
Defeature Size	Default (7.2617e-002 mm)
Capture Curvature	Yes
Curvature Min Size	Default (0.14523 mm)
Curvature Normal Angle	72.0°
Capture Proximity	Yes
Proximity Min Size	Default (0.14523 mm)

b) The settings

Figure 24 - The settings and the mesh of the thruster platform for optimization.

For the boundary conditions, cylindrical supports with free tangential movement were applied on the flats. The system is loaded with a 2N remote force applied to the connection of the thruster at the center of the platform representing the thruster weight which is the main load acting on the platform (Figure 25).

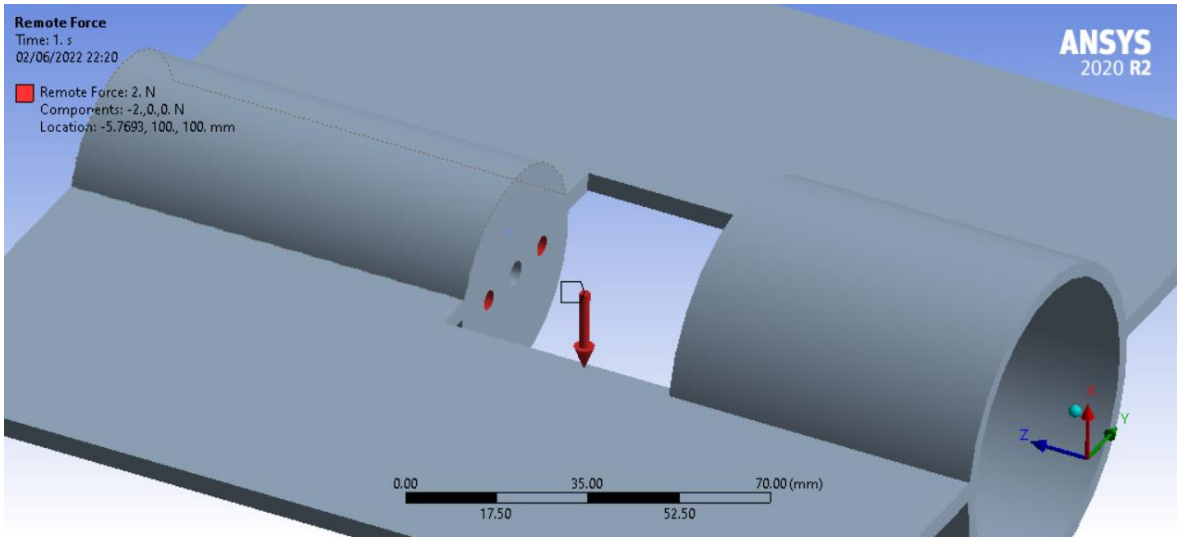

Figure 25 - The application of a remote force.

The default objective of minimal compliance and a response constraint of retaining 60 % of the mass were used. The results show the places where there is excessive material (Figure 26).

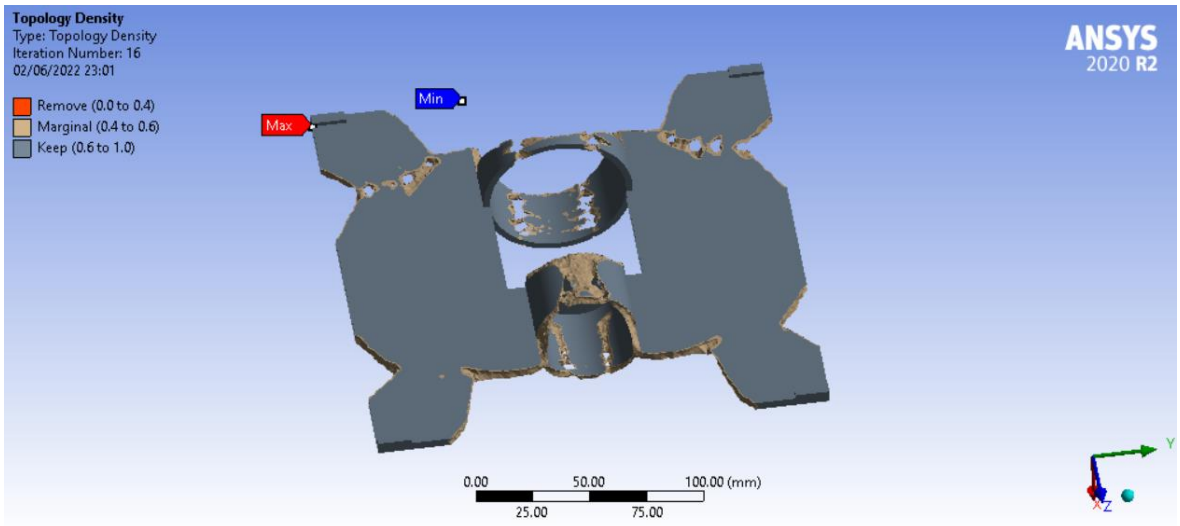

Figure 26 - The results of the topology optimization.

The geometry was changed in accordance with the results of the topology optimization. Only halves of the tubes were left which would enable a better access to the platform-thruster interface. Material on the sides of the platform was substantially reduced. The optimized geometry was statically analyzed with ANSYS to determine the performance. The results show that the platform is still oversized (Figure 27).

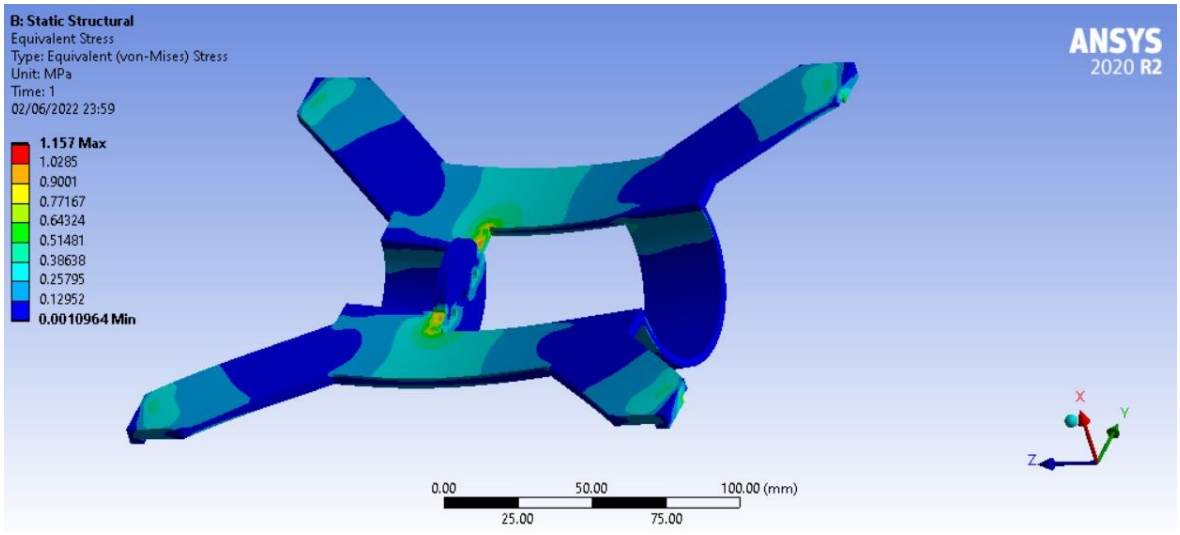

Figure 27 - The optimized thruster platform loaded with the weight of the thruster.

Instead of further topology optimization, it is solved rather by reducing the thickness of the platform. The final version for this iteration is shown in Figure 28. The optimized mass of the platform is 0.119 kg.

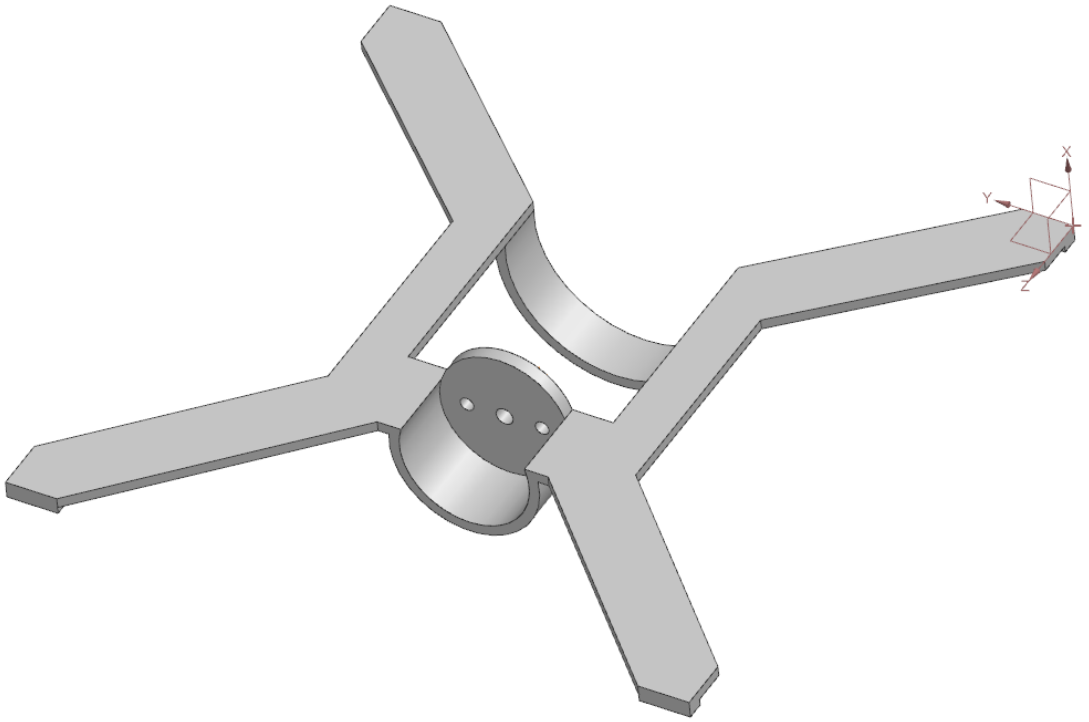

Figure 28 - The final thruster platform for iteration one.

5.2.4. Counterweight Platform

The requirements for the counterweight platform are much less strict. The purpose of this component is to add weight to the top of the system, so no topology optimization is necessary. The middle part of the platform is lowered so that the weight of the counterweight is transduced directly to the pivots and does not cause bending of the platform which would lead to a slight change in the platform dimension. Again, four flats

are required to connect with the knife edges. Also, a damper-platform interface is necessary at the bottom part of the platform.

The form of the actual weights is not crucial for the performance of the thrust stand. Larger blocks of 50 g each, and smaller blocks of 5 g each are chosen to enable fine tuning of the resultant weight.

5.2.5. Damper

The damping coefficient of an eddy current damper can be calculated as:

$$b = b_0 \cdot B^2 \cdot t \cdot A \cdot \sigma, \tag{25}$$

where B is the magnetic field, t is the thickness of the conductor, A is the area of the magnetic field intersected by the conductor, σ is the conductivity of the material of the conductor, and b_0 is a dimensionless coefficient to account for the shapes and sizes of the conductor and magnetic field. Typical values of b_0 are $0.25 - 0.4$ for a conductor 2-5 times larger than the magnetic field [16].

It is not necessary to fine-tune the damping coefficient since we are interested in the static behavior of the system rather than the dynamic. However, a framework calculation is necessary, so that the time to reaching an equilibrium is not overly long. Critical damping is calculated as:

$$b_c = 2 \cdot m \cdot \Omega. \tag{26}$$

In our case it is convenient to fist express the critical torsional damping:

$$b_{\varphi c} = 2 \cdot I_{Yp} \cdot \Omega \tag{27}$$

The critical damping for a linear damper placed on the counterweight platform will then be:

$$b_c = \frac{b_{\varphi c}}{l_W^2} = \frac{2 \cdot I_{Yp} \cdot \Omega}{l_W^2} \tag{28}$$
$$b_c = 5.381 \ \mathrm{kg \cdot s^{-1}}$$

This value is consistent with the value from the simulation in chapter 5.1.4, where the iteratively reached value of $5 \ \mathrm{kg \cdot s^{-1}}$ led to a slightly underdamped system.

The damper is designed as a copper plate passing through an electromagnet. An electromagnet is used to enable changing the damping constant in case of changing the configuration. For a $40\mathrm{x}40$ mm magnetic field intersecting a 2 mm thick, copper plate with a conductivity of $\sigma_{Cu} = 58.7 \cdot 10^6 \ \mathrm{S \cdot m^{-1}}$, a magnetic field of:

$$B = \sqrt{\frac{b_c}{b_0 \cdot t \cdot A \cdot \sigma}} \tag{29}$$
$$B = 0.266 \div 0.336 \ [\mathrm{T}]$$

is required to reach the critical damping. The copper plate is attached to the counterweight platform and the electromagnet is on the base platform.

5.2.6. Wiring and Tubing

The wires and the tubing are a connection between the stationary base and the moving thruster, necessary to supply electricity and a propellant. The wiring and tubing need to be designed for maximum compliance and/or maximum repeatability so that the parasitic forces are small and/or can be repeatably included in the calibration process. An exemplary thruster for the measurement contains a coupler for a tube with the inner diameter of $4\ \mathrm{mm}$. A $4.00\mathrm{x}6.00\ \mathrm{mm}$ silicone tube was selected for the propellant feed. The current supply to the thruster is $\sim 2\ \mathrm{mA}$. Copper wires with an intersection of $0.5\ \mathrm{mm}^2$ are more than sufficient for this application. Wires with silicone isolation with an outer diameter of $1.5\ \mathrm{mm}$ are used to ensure maximum compliance.

The elastic modulus of silicon found in the literature varies significantly. Typical values vary from $1\ \mathrm{MPa}$ to $50\ \mathrm{MPa}$ [23], but the range can be as wide as $0.005\ \mathrm{MPa}$ to $1900\ \mathrm{MPa}$ [24]. The value $E_{Silicon} = 50\ \mathrm{MPa}$ is used for the calculations, which is on the safe side. The elastic modulus of copper is approximately $E_{Cu} = 133\ 000\ \mathrm{MPa}$ [25]. The elastic modulus does not consider the fact, that the wire is composed of multiple tiny strings, which would lead to a decrease of the bending stiffness. The resistance is calculated assuming the tube and the wires are fixed on the stationary base and are connected to the thruster in a straight line.

The effective stiffness of the silicone tube can be calculated as:

$$k_{tube} = \frac{1}{\alpha_{11}} = \frac{3 \cdot E_{Silicon} \cdot Jz_{tube}}{l_T^3}, \tag{30}$$

where α_{11} is the influence factor, and the second moment of area of the tube can be calculated as:

$$Jz_{tube} = \frac{\pi \cdot (D_{tube}^4 - d_{tube}^4)}{64}. \tag{31}$$

Analogically the stiffness of a wire is:

$$k_{wire} = k_{Cu} + k_{Isolation} = \frac{3 \cdot E_{Cu} \cdot Jz_{wire}}{l_T^3} + \frac{3 \cdot E_{Silicon} \cdot Jz_{Isolation}}{l_T^3}, \tag{32}$$

and the second moments of inertia are:

$$Jz_{Isolation} = \frac{\pi \cdot (D_{wire}^4 - d_{wire}^4)}{64}, \tag{33}$$

and

$$Jz_{wire} = \frac{\pi \cdot d_{wire}^4}{64}. \tag{34}$$

The overall effective stiffnesses are:

$$k_{tube} = 1.197 \cdot 10^{-4}\ \mathrm{N \cdot mm^{-1}}$$

$$k_{wire} = (1.253 + 0.005) \cdot 10^{-4}\ \mathrm{N \cdot mm^{-1}} = 1.259 \cdot 10^{-4}\ \mathrm{N \cdot mm^{-1}}$$

The following equation applies to the resultant sensitivity of the thrust stand when the influence of the wiring and the tubing is included.

$$\frac{1}{s_R} = \frac{1}{s} + k_{tube} + 2 \cdot k_{wire}. \tag{35}$$

$$s_R = 1.015\ \text{mm} \cdot \text{N}^{-1}.$$

The wiring and the tubing account for 37.7 % decrease of the sensitivity. It should be noted, however, that the elastic modulus of silicone is probably largely overestimated, and the real effective stiffness of the tubing would be many times smaller. The effective elastic modulus of the wire would also likely be smaller, so this reduced sensitivity can be considered the absolutely worst-case scenario.

Other placements of the wiring and tubing can be considered to increase their compliance. For example, placements where the combination of torsion and bending acts on the wiring and tubing can be considered.

5.2.7. Displacement Sensor

The displacement sensor Micro-Epsilon ILD1420-50 would be attached with the vacuum chamber with the component developed in [6]. A flat plate attached to the link connecting two of the bottom pivots can be used as a reference point for the deflection measurement.

5.2.8. Vibration Isolation

The vibration isolation was designed to increase the natural frequencies (particularly the first two flexural modes) of the supporting construction and to reduce the external noise. Increasing the natural frequencies of the supporting construction is a relatively simple task since the mass is not an issue. To increase the natural frequencies, it is necessary to increase the stiffness. The supporting construction is shown in Figure 29.

Figure 29 – The supporting construction of the vacuum chamber [26].

The most natural way of increasing the stiffness is adding more links to reinforce the structure. A combination of horizontal and diagonal links can be used. The isolation from external noise can be achieved by putting a flexible underlay under the supporting construction. The Department of Aerospace engineering has a variety of foams and inflatable bags used for a modal analysis of an aircraft. The effects of the stiffness increase, and the noise isolation should be experimentally verified separately, and the appropriate stiffness increase, and the appropriate underlay should be specified according to the experimental results.

If neither should have the desired result, a vibration isolation inside the vacuum chamber would have to be designed. This, however, would bring several challenges. Most importantly, the attachment of the displacement sensor would have to be redesigned since the vibration of the vacuum chamber would cause relative motion of the isolated thrust stand and the sensor attached to the vacuum chamber.

5.2.9. Calibration

A detailed design of the calibration devise is a highly complicated task beyond the scope of this thesis. The general principle may be adopted from [22], where a cylindrical capacitor was used to produce forces in the range of 10^{-6}~10^{-9} N. The voltage between the inner and the outer electrode generated electrostatic force.

The calibration instrument is placed so that the calibrating force is colinear with the thrust force. This way the displacement caused by a calibration force accurately represents the displacement caused by the same thrust force.

5.2.10. Overall Performance

The designed components were put together and the performance was calculated. The mass properties of the main mechanical parts were taken from CAD and put into a table (Table 7). The mechanical components examined were the thruster platform, the counterweight platform, and the two pairs of pendulum arms. Parts were grouped in a logical manner with the masses of the components corresponding to each main part are added to it for a simpler mechanical analysis. The stationary parts were excluded from the analysis. The thruster platform has been slightly modified (an interface for the calibration instrument was added, and the material of the flats for knife edge placement was changed to tungsten-carbide).

The associated parts were:

- Thruster Platform – Thruster platform, part of the calibration instrument
- Counterweight Platform – Counterweight platform, the moving part of the damper
- Pendulum Arm 1 – 2 pendulum arms 6 pivots, 3 rods connecting the corresponding pivot pairs, the reference plate for displacement measurement
- Pendulum Arm 2 – 2 pendulum arms 6 pivots, 3 rods connecting the corresponding pivot pairs

Table 7 - The grouped parts with the corresponding mass properties.

		Position of the center of mass [mm]			
Part	Mass [kg]	X	Y	Z	I_Y [kg · mm^{-2}]
Thruster Platform	0.1346	-6.4825	100	103.8031	437.1484
Counterweight Platform	0.7144	587.118	100	100	2445.3772
Pendulum Arms 1	0.1514	307.5734	100	197.5173	7812.7597
Pendulum Arms 2	0.1499	310.7508	100	2.5	7659.7697

The performance of the system was tested in NX Motion. The thruster was added as a 0.2 kg mass point. First, the system was balanced, and after that the calculated parasitic forces were added as springs. The difference in the lengths of the pendulum arms was set at 0.5mm. The analysis was iteratively tuned, so that the sensitivity would be sufficient while the system is stable enough. The result of this iteration was adding a weight of 50 g to the upper platform to increase the counterweight.

The sensitivity with such settings is:

$$s = 2.312 \text{ m} \cdot \text{N}^{-1}.$$

With parasitic forces, the sensitivity decreases to:

$$s = 1.089\ \mathrm{m} \cdot \mathrm{N}^{-1}.$$

The measured thrusts ranges would be $2\ \mathrm{mN} - 100\ \mu\mathrm{N}$. To achieve an accuracy of $\pm 10\ \%$ for the lowest thrust, we need to be able to measure the displacement

$$0.1 \cdot T \cdot s = 0.1 \cdot 100 \cdot 1.089 = \pm 10.89\ [\mu\mathrm{m}].$$

This is well within the capabilities of the displacement sensor. However, if the worst-case scenario predictions were true, the amplitude of the vibrations would be just under $50\ \mu\mathrm{m}$, even though the actual value is likely smaller (the assumption of a square wave increases the calculated amplitude $2.47\mathrm{x}$ compared to a sine wave). The vibration isolation should decrease the amplitude of vibration below $10.89\ \mu\mathrm{m}$ to achieve the desired accuracy.

Even though the sensitivity is sufficient, the parasitic forces reduce the sensitivity more than $2\mathrm{x}$. For that reason, the reduction of those forces could take place in the further iterations. This would include reconsideration of the placement of the wiring and tubing, carefully picking a tube made of a silicone with a low elastic modulus, and/or any ways of decreasing the inequality of the length of the pendulum arms. The CAD model of the thrust stand is shown in figure

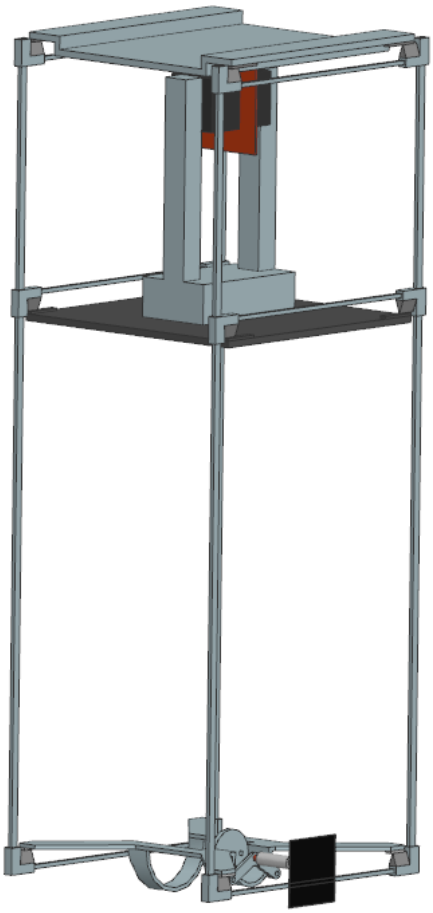

Figure 30 - The CAD model of the thrust stand.

6. Conclusion

The aim of this thesis was to research the practically used approaches to micro-thrust measurement. Approaches utilizing various physical laws were found and their key parameters were examined.

Then the aim was to determine the working conditions and construction limitations for micro-thrust measurement at the facility of the Department of Aerospace Engineering at FME CTU. An experiment was set to measure the time course of accelerations in the X, Y, and Z direction during various external conditions.

The final goal was to apply the gained knowledge to create a preliminary design of a thrust stand suitable for the facility.

The hanging pendulum principle was selected as the most appropriate for the given working conditions and construction limitations particularly for its low sensitivity to the external conditions. The main disadvantage of low deflection values is compensated by a high precision displacement sensor combined with vibration isolation.

A preliminary design was created. The influence of potential inaccuracies of individual components on the resultant sensitivity was analyzed. Based on the analysis, the thrust stand should still give sufficient sensitivity for the measurement of the given thrust ranges, although vibration isolation might be needed.

The concept proved to be feasible for micro-thrust measurement in the given conditions. The next steps in full development of the thrust stand would include experimental verification of the lowest pressure that can be achieved with a running thruster, experimental verification of the vibration isolation, and next iterations of the design based on the results. Also, a detailed design of the calibration instrument would be necessary.

References

[1] POLK, James, Anthony PANCOTTI, Thomas HAAG, Scott KING, Mitchell WALKER, Joseph BLAKELY a John ZIEMER. Recommended Practice for Thrust Measurement in Electric Propulsion Testing. *Journal of Propulsion and Power*. 2017, **33**(3), 539-555. ISSN 0748-4658. Dostupné z: doi:10.2514/1.B35564

[2] THOREAU, Peter a Justin LITTLE. Development of the SPACE Lab Thrust Stand for Millinewton Thrust Measurement. *International Electric Propulsion Conference*. 2019, **36**(715).

[3] WANG, Anliang, Hongwei WU, Haibin TANG, Yu LIU a Xing LIANG. Development and testing of a new thrust stand for micro-thrust measurement in vacuum conditions. *Vacuum* [online]. 2013, **91**, 35-40 [cit. 2022-06-05]. ISSN 0042207X. Dostupné z: doi:10.1016/j.vacuum.2012.10.013

[4] HEY, Franz, Andreas KELLER, Claus BRAXMAIER, Martin TAJMAR, Ulrich JOHANN a Dennis WEISE. Development of a Highly Precise Micronewton Thrust Balance. *IEEE Transactions on Plasma Science* [online]. 2015, **43**(1), 234-239 [cit. 2022-06-05]. ISSN 0093-3813. Dostupné z: doi:10.1109/TPS.2014.2377652

[5] MOELLER, Trevor a Kurt POLZIN. Thrust stand for vertically oriented electric propulsion performance evaluation. *Review of Scientific Instruments* [online]. 2010, **81**(11) [cit. 2022-06-05]. ISSN 0034-6748. Dostupné z: doi:10.1063/1.3502463

[6] BOHATA, Lukáš. *Design of validation procedure of ion thruster demonstator*. Prague, 2020. Bachelor's Thesis. Czech Technical University in Prague. Vedoucí práce Mgr. Jaroslav Kousal, Ph.D.

[7] SPETHMANN, A., T. TROTTENBERG a H. KERSTEN. Instrument for spatially resolved simultaneous measurements of forces and currents in particle beams. *Review of Scientific Instruments* [online]. 2015, **86**(1) [cit. 2022-06-04]. ISSN 0034-6748. Dostupné z: doi:10.1063/1.4905534

[8] LinACE vs. LVDT transducer. In: *RLS: rotary and linear motion sensors* [online]. 2022 [cit. 2022-06-04]. Dostupné z: https://www.rls.si/eng/encoder-handbook/linace-vs-lvdt-transducer?gclid=Cj0KCQjwheyUBhD-ARIsAHJNM-M3qarMTpj2Cv-CLG8Mh2Bit1SnDgq4IWMF2p1Myo_8JnU5Qb7CUiYaAmHxEALw_wcB

[9] Single-Channel RVDT Sensors | Sensata Technologies. In: *Sensata Technologies: Sensing is What We Do* [online]. 2022 [cit. 2022-06-04]. Dostupné z: https://www.sensata.com/products/position-sensors-encoders/single-channel-rvdt-sensors

[10] Precision Capacitive Position Sensor – Model 4810. In: *Capacitive Sensors, Vibrating Sample Magnetometers - MicroSense* [online]. 2022 [cit. 2022-06-04]. Dostupné z: http://www.microsense.net/products-position-sensors-microsense-4800.htm

[11] TYLER ESTLER, W. High-accuracy displacement interferometry refin air. *Applied Optics* [online]. 1985, **24**(6) [cit. 2022-06-04]. ISSN 0003-6935. Dostupné z: doi:10.1364/AO.24.000808

[12] GAMERO-CASTAñO, Manuel. A torsional balance for the characterization of microNewton thrusters. *Review of Scientific Instruments* [online]. 2003, **74**(10), 4509-4514 [cit. 2022-06-04]. ISSN 0034-6748. Dostupné z: doi:10.1063/1.1611614

[13] Dax--optoNCDT-1420--en.html. In: *Snímače | Micro-Epsilon* [online]. 2022 [cit. 2022-06-04]. Dostupné z: https://www.micro-epsilon.cz/download/products/cat-optoncdt/dax--optoNCDT-1420--en.html#page=2&zoom=Fit

[14] Technical Guide - PHOTOELECTRIC SENSORS. In: *Home - Panasonic* [online]. Panasonic Industry Co., Ltd. [cit. 2022-06-04]. Dostupné z: https://www3.panasonic.biz/ac/ae/service/tech_support/fasys/tech_guide/data/photoelectric_e.pdf

[15] SODANO, H. Eddy Current Damping in Structures. *The Shock and Vibration Digest* [online]. 2004, **36**(6), 469-478 [cit. 2022-06-05]. ISSN 0583-1024. Dostupné z: doi:10.1177/0583102404048517

[16] ZUO, Lei, Xiaoming CHEN a Samir NAYFEH. Design and Analysis of a New Type of Electromagnetic Damper With Increased Energy Density. *Journal of Vibration and Acoustics* [online]. 2011, **133**(4) [cit. 2022-06-05]. ISSN 1048-9002. Dostupné z: doi:10.1115/1.4003407

[17] LI, Huan, Yancheng LI a Jianchun LI. Negative stiffness devices for vibration isolation applications: A review. *Advances in Structural Engineering* [online]. 2020, **23**(8), 1739-1755 [cit. 2022-06-05]. ISSN 1369-4332. Dostupné z: doi:10.1177/1369433219900311

[18] Vibration Isolation | LIGO Lab | Caltech. In: *LIGO Lab | Caltech | MIT* [online]. Pasadena, CA: LIGO Caltech [cit. 2022-06-05]. Dostupné z: https://www.ligo.caltech.edu/page/vibration-isolation

[19] CHOI, In-Mook a Ian ROBINSON. An analysis and design of the mechanical characteristics of the knife edges used in the NPL watt balance. *Metrologia* [online]. 2014, **51**(2), 114-122 [cit. 2022-06-06]. ISSN 0026-1394. Dostupné z: doi:10.1088/0026-1394/51/2/S114

[20] Knife Edges and Pivots. In: *Scribd Home* [online]. SCRIBD, 2019 [cit. 2022-06-06]. Dostupné z: https://www.scribd.com/document/400025347/Knife-Edges-and-Pivots

[21] NAGAO, Naoki, Shigeru YOKOTA, Kimiya KOMURASAKI a Yoshihiro ARAKAWA. Development of a Dual Pendulum Thrust Stand for Hall Thrusters. In: *43rd AIAA/ASME/SAE/ASEE Joint Propulsion Conference & Exhibit* [online]. Reston, Virigina: American Institute of Aeronautics and Astronautics, 2007, s. - [cit. 2022-06-06]. ISBN 978-1-62410-011-6. Dostupné z: doi:10.2514/6.2007-5298

[22] QI, Yong, Le SONG a Yin HUANG. A Micro Force Measuring System Based on Static Electric Field Theory. *Applied Mechanics and Materials* [online]. 2012, **203**, 99-102 [cit. 2022-06-06]. ISSN 1662-7482. Dostupné z: doi:10.4028/www.scientific.net/AMM.203.99

[23] Properties: Silicone Rubber. In: *Material Science | News | Materials Engineering | News* [online]. AZOM, 2000 [cit. 2022-06-06]. Dostupné z: https://www.azom.com/properties.aspx?ArticleID=920

[24] MatWeb - The Online Materials Information Resource. In: *Online Materials Information Resource - MatWeb* [online]. MatWeb, 1996 [cit. 2022-06-06]. Dostupné z: https://www.matweb.com/errorUser.aspx?msgid=2&ckck=nocheck

[25] Properties: An Introduction to Copper. In: *Material Science | News | Materials Engineering | News* [online]. AZOM, 2000 [cit. 2022-06-06].

[26] KOUBEK, Matěj. *Validation of Temperatures in a Thermal-Vacuum Chamber*. Prague, 2021. Master's Thesis. Czech Technical University in Prague. Vedoucí práce Ing. Jaromír Kučera.

List of Figures

List of Tables

APPENDIX 1 – Calibration Chart of the Accelerometers

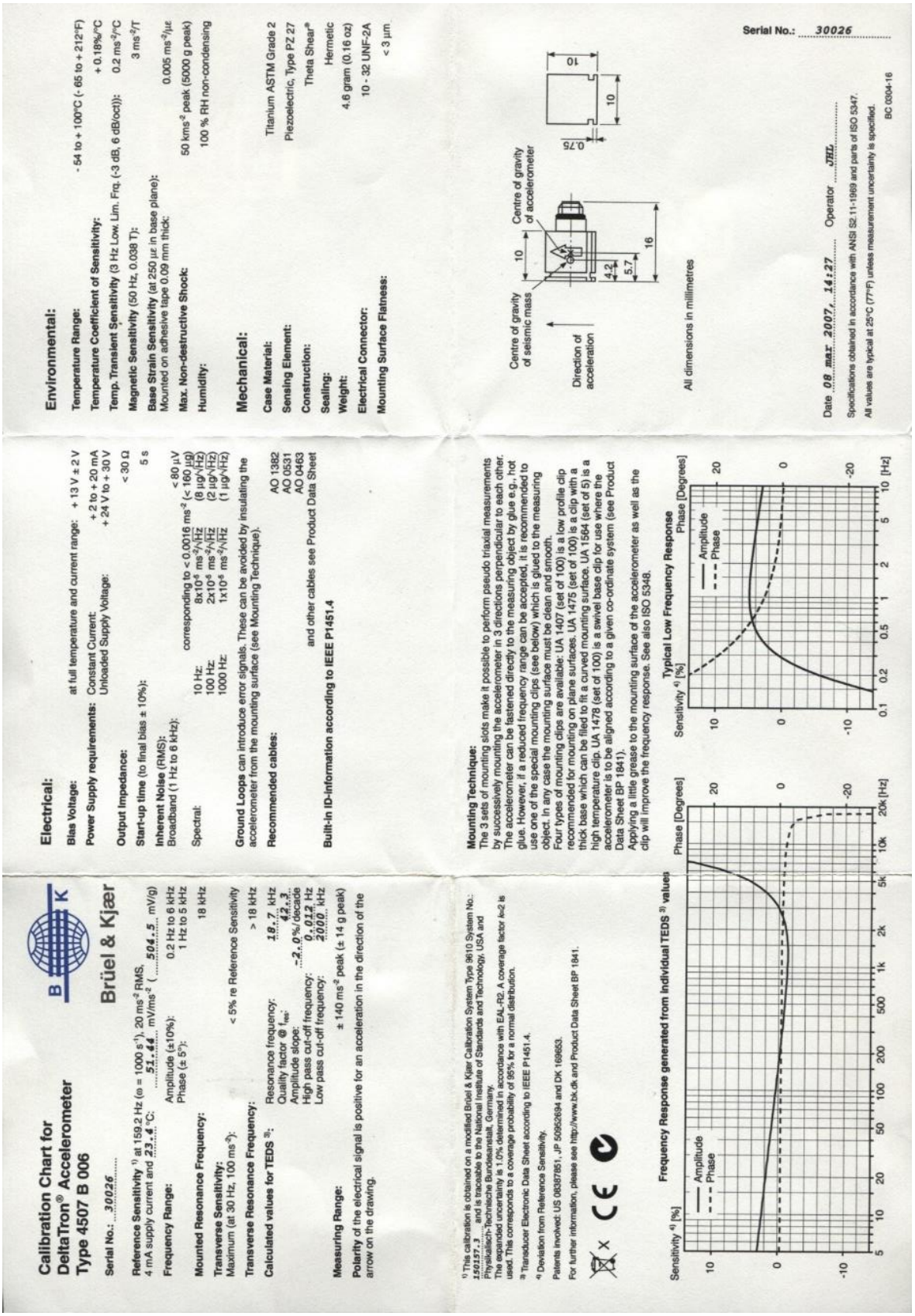

Calibration Chart for DeltaTron® Accelerometer
Type 4507 B 006

Serial No.: 30026

Brüel & Kjær

Reference Sensitivity [1] at 159.2 Hz (ω = 1000 s⁻¹), 20 ms⁻² RMS, 4 mA supply current and 23.4 °C: 51.44 mV/ms⁻² (504.5 mV/g)

Frequency Range: Amplitude (±10%): 0.2 Hz to 6 kHz; Phase (± 5°): 1 Hz to 5 kHz

Mounted Resonance Frequency: 18 kHz

Transverse Sensitivity: Maximum (at 30 Hz, 100 ms⁻²): < 5% re Reference Sensitivity

Transverse Resonance Frequency: > 18 kHz

Calculated values for TEDS [3]: Resonance frequency: 18.7 kHz; Quality factor @ f_res: 42.3; Amplitude slope: -2.0 %/decade; High pass cut-off frequency: 0.012 Hz; Low pass cut-off frequency: 2000 kHz

Measuring Range: ± 140 ms⁻² peak (± 14 g peak)

Polarity of the electrical signal is positive for an acceleration in the direction of the arrow on the drawing.

[1] This calibration is obtained on a modified Brüel & Kjær Calibration System Type 9610 System No.: 1501572 and is traceable to the National Institute of Standards and Technology, USA and Physikalisch-Technische Bundesanstalt, Germany.
The expanded uncertainty is 1.0% determined in accordance with EAL-R2. A coverage factor k=2 is used. This corresponds to a coverage probability of 95% for a normal distribution.
[3] Transducer Electronic Data Sheet according to IEEE P1451.4.
[4] Deviation from Reference Sensitivity.
Patents involved: US 06387851, JP 50952694 and DK 169863.
For further information, please see http://www.bk.dk and Product Data Sheet BP 1841.

Frequency Response generated from individual TEDS [3] values

Sensitivity [4] [%] / Phase [Degrees]
Amplitude
Phase
5 10 20 50 100 200 500 1k 2k 5k 10k 20k [Hz]

Electrical:

Bias Voltage:	at full temperature and current range:	+ 13 V ± 2 V
Power Supply requirements:	Constant Current:	+ 2 to + 20 mA
	Unloaded Supply Voltage:	+ 24 V to + 30 V
Output Impedance:		< 30 Ω
Start-up time (to final bias ± 10%):		5 s
Inherent Noise (RMS):		
Broadband (1 Hz to 6 kHz):		< 80 µV
Spectral:	corresponding to < 0.0016 ms⁻² (< 160 µg)	
10 Hz:	8x10⁻⁶ ms⁻²/√Hz (8 µg/√Hz)	
100 Hz:	2x10⁻⁶ ms⁻²/√Hz (2 µg/√Hz)	
1000 Hz:	1x10⁻⁶ ms⁻²/√Hz (1 µg/√Hz)	

Ground Loops can introduce error signals. These can be avoided by insulating the accelerometer from the mounting surface (see Mounting Technique).

Recommended cables: AO 1382, AO 0531, AO 0463 and other cables see Product Data Sheet

Built-in ID-information according to IEEE P1451.4

Mounting Technique:
The 3 sets of mounting slots make it possible to perform pseudo triaxial measurements by successively mounting the accelerometer in 3 directions perpendicular to each other. The accelerometer can be fastened directly to the measuring object by glue e.g., hot glue. However, if a reduced frequency range can be accepted, it is recommended to use one of the special mounting clips (see below) which is glued to the measuring object. In any case the mounting surface must be clean and smooth.
Four types of mounting clips are available: UA 1407 (set of 100) is a low profile clip recommended for mounting on plane surfaces. UA 1475 (set of 100) is a clip with a thick base which can be filed to fit a curved mounting surface. UA 1564 (set of 5) is a high temperature clip. UA 1478 (set of 100) is a swivel base clip for use where the accelerometer is to be aligned according to a given co-ordinate system (see Product Data Sheet BP 1841).
Applying a little grease to the mounting surface of the accelerometer as well as the clip will improve the frequency response. See also ISO 5348.

Typical Low Frequency Response

Sensitivity [4] [%] / Phase [Degrees]
Amplitude
Phase
0.1 0.2 0.5 1 2 5 10 [Hz]

Environmental:

Temperature Range:	- 54 to + 100°C (- 65 to + 212°F)
Temperature Coefficient of Sensitivity:	+ 0.18%/°C
Temp. Transient Sensitivity (3 Hz Low. Lim. Frq. (-3 dB, 6 dB/oct)):	0.2 ms⁻²/°C
Magnetic Sensitivity (50 Hz, 0.038 T):	3 ms⁻²/T
Base Strain Sensitivity (at 250 µε in base plane): Mounted on adhesive tape 0.09 mm thick:	0.005 ms⁻²/µε
Max. Non-destructive Shock:	50 kms⁻² peak (5000 g peak)
Humidity:	100 % RH non-condensing

Mechanical:

Case Material:	Titanium ASTM Grade 2
Sensing Element:	Piezoelectric, Type PZ 27
Construction:	Theta Shear®
Sealing:	Hermetic
Weight:	4.6 gram (0.16 oz)
Electrical Connector:	10 - 32 UNF-2A
Mounting Surface Flatness:	< 3 µm

Centre of gravity of seismic mass
Direction of acceleration
10
Centre of gravity of accelerometer
4.2
5.7
16
10
10
0.75

All dimensions in millimetres

Serial No.: 30026

Date 08 mar 2007, 14:27 Operator JHL

Specifications obtained in accordance with ANSI S2.11-1969 and parts of ISO 5347.
All values are typical at 25°C (77°F) unless measurement uncertainty is specified.

BC 0304-16